

The Laplacian Mechanism Improves Transformers by Reshaping Token Geometry

Yuchong Zhang^{1,2} Vardan Papyan^{3,1,2}

Abstract

Transformers leverage attention, the residual connection, and layer normalization to control the variance of token representations. We propose to modify attention into a Laplacian mechanism that gives the model more direct control over token variance. We conjecture that this helps transformers achieve the ideal token geometry. To investigate our conjecture, we first show that incorporating the Laplacian mechanism into transformers induces consistent improvements across benchmarks in computer vision and language. Next, we study how the Laplacian mechanism impacts the geometry of token representations using various tools: 1) principal component analysis, 2) cosine similarity metric, 3) analysis of variance, and 4) Neural Collapse metrics. Our investigation shows that the Laplacian mechanism reshapes token embeddings toward a geometry of maximal separability: tokens collapse according to their classes, and the class means exhibit Neural Collapse.

1. Introduction

1.1. Motivation

The transformer architecture has achieved remarkable success across a wide range of tasks since its introduction by [Vaswani et al. \(2017\)](#). A transformer tokenizes its input into a sequence of tokens and processes these tokens using a sequence of blocks. The core components of each block are attention, the residual connection ([He et al., 2015](#)), and layer normalization ([Ba et al., 2016](#)). Together, they shape how tokens move in the representation space.

Softmax self-attention can be viewed as a learned averaging

¹Department of Computer Science, University of Toronto, Ontario, Canada ²Vector Institute, Toronto, Ontario, Canada

³Department of Mathematics, University of Toronto, Ontario, Canada. Correspondence to: Yuchong Zhang <yuchongz.zhang@mail.utoronto.ca>.

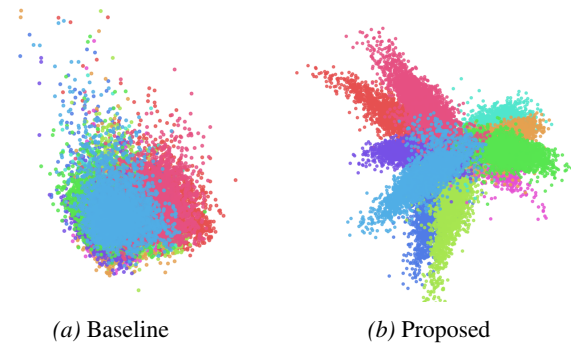


Figure 1. The proposed modification cleanly separates tokens into clusters according to class. Each colour corresponds to one class.

operator. For each token, attention computes a contextual mean of tokens, where the weights are determined by token similarities. The residual connection then adds this mean back to each token. This update changes the ratio between the magnitude of the mean and the variance. Layer normalization then projects the tokens back onto a sphere, thereby controlling the variance of the tokens. This process occurs in all blocks, driving token representations toward some geometric configuration at the final layer.

What geometry should token representations follow? For standard classifiers, [Papyan et al. \(2020\)](#) showed that as training approaches zero error, the final-layer representations exhibit a distinctive geometry—termed **Neural Collapse (NC)**—with four defining properties:

- NC1** Final-layer features collapse to their class means.
- NC2** The class means converge to a simplex equiangular tight frame (ETF).
- NC3** The linear classifier weights align with the corresponding class means.
- NC4** The classifier predicts each class via nearest-class-mean decision boundaries.

While NC has been extensively studied in convolutional networks for image classification ([Papyan et al., 2020; Han et al., 2022](#)), transformers present a markedly different setting: inputs are tokenized.

A related line of work studies *rank collapse*, where token embeddings become low-rank and can collapse toward a single point. In particular, Geshkovski et al. (2024) proved theoretically that self-attention collapses tokens into various geometries depending on the initial conditions. These works do not identify an optimal geometry, but they suggest that the rank and variance of tokens are central to the geometry induced by attention dynamics.

Standard transformers control token variance in a seemingly indirect manner: by first changing the mean’s magnitude relative to variance and then normalizing. Thus, we are motivated to conjecture: **giving the transformer more direct control over token variance can help it attain the ideal token geometry.**

1.2. Contributions

To investigate our conjecture, we first introduce the Laplacian mechanism, a simple modification to attention that computes the difference between each token and its corresponding contextual mean. This allows the model to directly decrease or increase the variance of tokens via the residual connection (Section 2). Next, we incorporate the Laplacian mechanism into standard transformers and evaluate on both vision and language datasets. Our experiments show consistent performance improvements (Section 3). We then study the geometry of token representations (Section 4) in vision transformers trained for image classification using PCA, cosine similarity metric, analysis of variance, and Neural Collapse metrics. We find that the Laplacian mechanism promotes a geometry that admits maximal separability between classes. We term this geometry Neural Token Collapse (NTC), which is characterized by:

NTC0 Tokens in the same sequence collapse.

NTC1 Tokens in the same class collapse to the class mean.

NTC2-4 The class means and classifier weights satisfy NC2, NC3, and NC4.

We formally define NTC in Section 5.

2. Proposed Architecture Modification

2.1. Standard Attention Mechanism

Consider a sequence of T token embeddings (x_1, \dots, x_T) with each $x_i \in \mathbb{R}^d$, collected into a matrix $X \in \mathbb{R}^{T \times d}$. Attention projects X into queries, keys, and values using trainable matrices $W_Q, W_K, W_V \in \mathbb{R}^{d \times d_k}$:

$$Q = XW_Q, \quad K = XW_K, \quad V = XW_V.$$

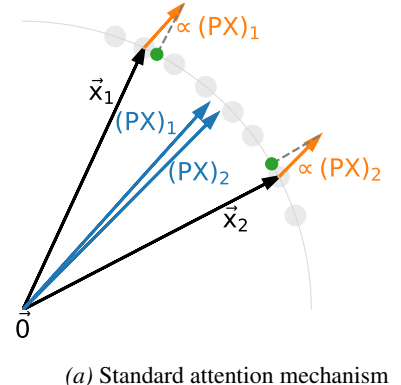
It then computes scaled dot-product weights and outputs a weighted sum of the values:

$$P = \text{softmax}\left(\frac{QK^\top}{\sqrt{d_k}}\right), \quad \text{Attention}(X) = PV. \quad (1)$$

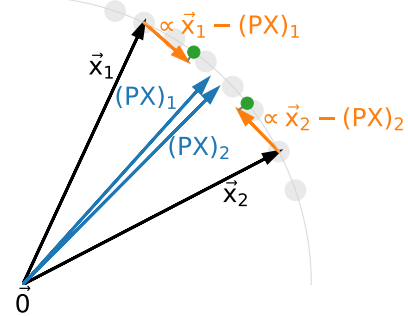
Building on this definition, multi-head attention (MHA) computes h attention heads in parallel, concatenates their outputs, then applies a trainable projection matrix $W_o \in \mathbb{R}^{hd_k \times d}$. The result is added back to the input via a residual connection (He et al., 2015):

$$\tilde{X} = \text{LayerNorm}(X), \quad X' = X + \text{MHA}(\tilde{X}). \quad (2)$$

After this residual update, the token embeddings are passed through layer normalization, which projects the tokens onto a sphere with radius \sqrt{d} . This process repeats at each layer.



(a) Standard attention mechanism



(b) Proposed Laplacian mechanism

Figure 2. The Laplacian mechanism changes the variance of token embeddings more directly.

Interpretation. Equation 2 changes how large the tokens’ mean is relative to their variance, and the subsequent normalization regulates the variance of tokens. Figure 2a illustrates an example of decreasing token variance: token embeddings \vec{x}_1, \vec{x}_2 (black arrows) are shifted by their attention-weighted means $(PX)_1, (PX)_2$ (blue arrows) along the orange arrows. After projection, the tokens become closer and the variance decreases.

2.2. The Laplacian Mechanism

We modify the standard attention mechanism into a *Laplacian mechanism*, denoted by \mathbf{L} :

$$P = \text{softmax}\left(\frac{QK^\top}{\sqrt{d_k}}\right), \quad \mathbf{L}(X) = V - PV. \quad (3)$$

The name “Laplacian” will be explained in Section 6.

Interpretation. \mathbf{L} computes the difference between tokens and their average. If every attention head is replaced with \mathbf{L} , then Equation 2 allows the model to directly decrease (or increase, since W_o can change the sign of the update) the variance of tokens without relying on the redundant radial movement later canceled by projection. Figure 2b illustrates an example of decreasing token variance: token embeddings \vec{x}_1, \vec{x}_2 (black arrows) move directly towards the means $(PV)_1, (PV)_2$ (blue arrows) along the variance direction (orange arrows). The green points are the projected tokens, which end up much closer together with normalization playing only a minor role. We provide empirical evidence for this interpretation in Appendix D.

2.3. Mixing Both Mechanisms

We propose incorporating the Laplacian mechanism into transformers by the following simple strategy: in every layer, use the Laplacian for k heads and standard attention for the remaining heads for some fixed $k < h$, where h is the total number of heads. This strategy is straightforward to implement and introduces no additional trainable parameters. Moreover, it allows us to study the impact of the Laplacian heads by varying k in each layer. We describe some alternative strategies we have tried in Appendix E.

Interpretation. This setup allows the standard attention heads to update the mean of tokens, while the Laplacian heads gives the model more direct control over the variance of tokens, thereby giving the model greater flexibility to steer tokens toward the ideal geometry.

3. The Laplacian Mechanism Improves Transformers

3.1. Image Classification

Our experiments used the DeiT-3 family of vision transformers (Touvron et al., 2022), a strong baseline for image classification. We focused on the ViT-B model, which has 12 blocks with 12 attention heads per block. Following the strategy described earlier, we replaced k heads with the Laplacian mechanism in each block for $k \in \{0, 3, 6, 9, 11, 12\}$, where $k = 0$ corresponds to the baseline ViT-B. For brevity, we shall refer the baseline as “ViT-B” and the model with k Laplacian heads in each layer as “ViT-B- k L”. We trained

all models on CIFAR10, CIFAR100 (Krizhevsky, 2009), and ImageNet-1k (Deng et al., 2009) using the exact same training recipe and hyper-parameters.

DeiT-3 employs stochastic depth (Huang et al., 2016), a regularization technique where each block is skipped with some probability $0 < p < 1$ (called the drop path rate). For each dataset, we trained models using drop path rates $p \in \{0.1, 0.3, 0.4\}$. Full details of the training setup are included in Appendix B.

Table 2. Top-1 accuracy (%), mean \pm std. Best in bold, second best underlined. k L denotes model with k Laplacian heads.

Model	CIFAR10	CIFAR100	ImageNet
Baseline	95.35 ± 0.16	75.12 ± 0.46	81.45 ± 0.08
3L	95.38 ± 0.17	75.81 ± 0.14	82.73 ± 0.19
6L	95.36 ± 0.10	76.39 ± 0.26	<u>82.70 ± 0.02</u>
9L	95.76 ± 0.30	76.80 ± 0.39	82.47 ± 0.08
11L	95.88 ± 0.14	76.83 ± 0.26	82.40 ± 0.12
12L	<u>95.86 ± 0.10</u>	77.04 ± 0.40	82.32 ± 0.07

Table 2 compares top-1 test accuracy for models with varying numbers of Laplacian heads k , using for each dataset the drop path rate that maximized baseline performance. Across all datasets, adding Laplacian heads improves accuracy for every choice of k . On CIFAR10 and CIFAR100, the improvement increases monotonically with k . We do not observe this pattern on ImageNet, consistent with our intuition that hard tasks benefit from both Laplacian heads and attention (Section 2.3). Nevertheless, the $> 1\%$ improvement on ImageNet indicates that Laplacian heads could be effective on large datasets. Figure 3 further shows that these improvements persist across different drop path rates.

3.2. Autoregressive Next-token Prediction

We trained decoder-only transformers for autoregressive next-token prediction. Specifically, we took a GPT-2 style transformer with 561 million parameters as the baseline. The model has 10 heads per block, and we trained models with k Laplacian heads in each block, for $k \in \{0, 1, 7, 5, 3, 10\}$. We used a three-stage training process, following Karpathy (2025): pre-training on 11.2 billion tokens from FineWebEdu (Lozhkov et al., 2024) followed by mid-training and supervised finetuning (SFT) on chat and task-mixture data. We then evaluated the SFT model on ARC-Easy, ARC-Challenge (Clark et al., 2018), MMLU (Hendrycks et al., 2021), GSM8K (Cobbe et al., 2021), and HumanEval (Chen et al., 2021). We report pass@10 accuracy for GSM8K and HumanEval and zero-shot accuracy for the other benchmarks. We also report the average performance across all tasks as a single metric to reflect the overall model qualities. More details of the

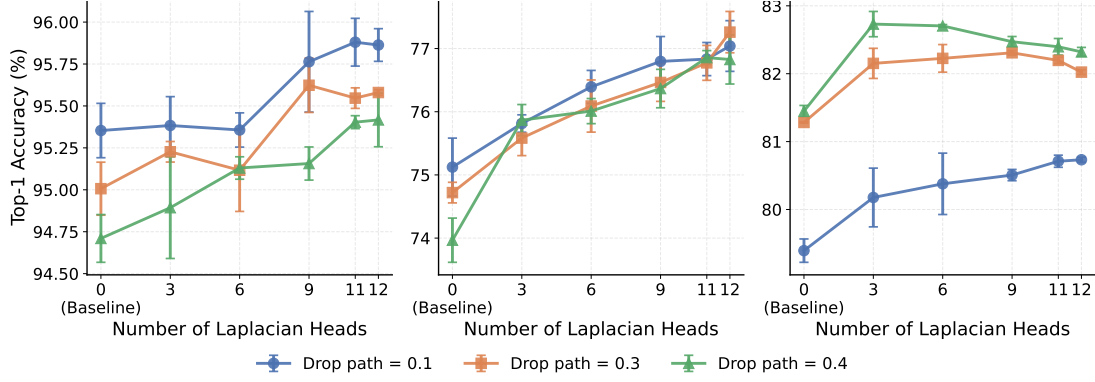


Figure 3. The Laplacian mechanism is effective across different drop path rates.

 Table 1. Accuracies (%) on reasoning and code benchmarks. \uparrow indicates higher is better.

Model	ARC-Easy \uparrow	ARC-Challenge \uparrow	MMLU \uparrow	GSM8K \uparrow	HumanEval \uparrow	Avg \uparrow
Random	25.00	25.00	25.00	0.00	0.00	–
Baseline (no Laplacian heads)	39.60	28.75	31.41	22.29	<u>12.80</u>	26.97
1 Laplacian head	43.86	30.29	33.00	23.81	<u>12.80</u>	28.75
3 Laplacian heads	42.26	29.61	33.23	24.26	12.20	28.31
5 Laplacian heads	48.78	35.07	33.17	<u>24.87</u>	<u>12.80</u>	30.94
7 Laplacian heads	44.91	<u>32.85</u>	<u>33.45</u>	21.99	14.63	29.57
9 Laplacian heads	<u>46.55</u>	32.42	33.56	23.73	14.63	30.18
10 Laplacian heads	46.13	30.97	32.99	23.12	10.98	30.08

experiments are in Appendix B.

Table 1 shows that adding Laplacian heads produces noticeably higher average accuracy than the baseline for all tested choices of k . On the multiple-choice benchmarks (ARC and MMLU), all variants outperformed the baseline, with $k = 5$ achieving the largest gain on ARC-Easy (+9.18%) and ARC-Challenge (+6.32%). On GSM8K, most Laplacian models also improved over the baseline, with $k = 5$ giving the best result (+2.58%). On HumanEval, performance is generally comparable to the baseline, with $k = 9$ and 7 performing the best. We note that next-token prediction is inherently different from supervised classification because the same sequence prefix can have different target next tokens. Thus, our results suggest that the Laplacian mechanism could help generative tasks such as reasoning and code.

4. The Laplacian Mechanism Reshapes Token Geometry

Next, we apply various tools to study the impact of Laplacian heads on token distributions and geometry in vision transformers from Section 3.1.

4.1. Principal Component Analysis (PCA) of Token Embeddings

We apply PCA to a batch of sequences of token embeddings and project them onto \mathbb{R}^2 using the top-two principal com-

ponents, as defined in Algorithm 1. Tokens belonging to the same class are visualized in the same color.

Figure 1a illustrates the PCA projection of the last-block output token embeddings for ViT-B and ViT-B-12L trained on CIFAR-10. For ViT-B, tokens from different classes overlap and exhibit no clear geometry. In contrast, token embeddings of ViT-B-12L form well-separated clusters. Visually, we observe that as the number of Laplacian heads increases, different classes appear more separated (see Appendix C). A similar pattern can be seen for models trained on CIFAR-100 and ImageNet.

4.2. Analysis of Variance (ANOVA) of Token Embeddings

We describe the distribution of token embeddings by formalizing the notion of “token variance”. We consider a dataset D with N samples and C classes, where class c contains N_c samples so that $N = \sum_{c=1}^C N_c$. Each data point is tokenized into a sequence of T tokens. For $1 \leq c \leq C$, $1 \leq i \leq N_c$, and $1 \leq t \leq T$, let $X_{t,i,c}$ denote the embedding of the t -th token of the i -th sample in class c .

4.3. Token Means

We first define several means. For each data point we compute the *sequence token mean*, which is the average of its T

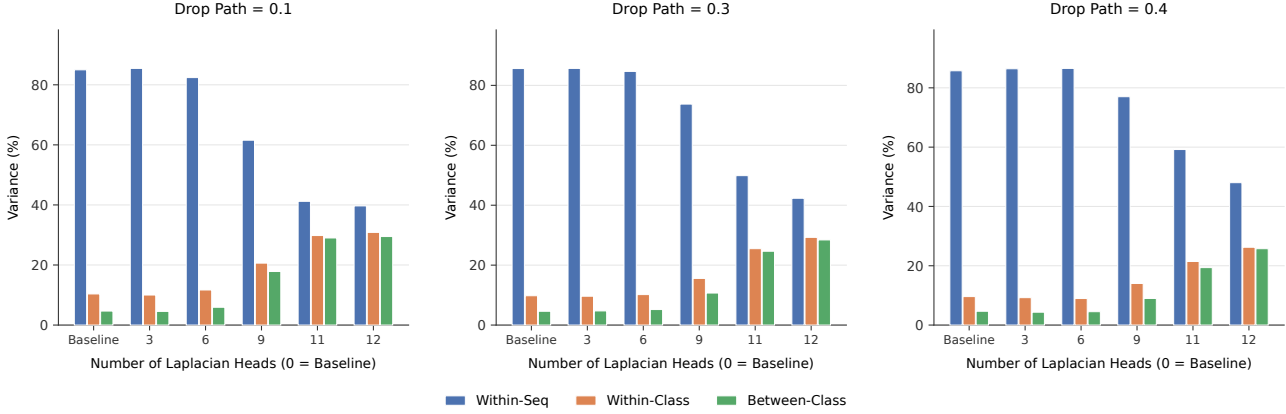


Figure 4. The Laplacian heads shift the total variance to BetweenClassVar, inducing stronger between-class separability.

token embeddings:

$$\mu_{i,c} = \mathbf{Ave}_t X_{t,i,c}.$$

For each class, we compute the *class token mean*, obtained by averaging the sequence means over all N_c data points in that class:

$$\mu_c = \mathbf{Ave}_i \mu_{i,c} = \mathbf{Ave}_t X_{t,i,c}.$$

Finally, we compute the *global token mean* by averaging the class means over all C classes:

$$\mu_G = \mathbf{Ave}_c \mu_c = \mathbf{Ave}_t X_{t,i,c}.$$

4.4. Token Variances

Using $\mu_{i,c}$, μ_c , and μ_G , we define several measures of variance that quantify different aspects of token distribution.

The *within-sequence variance* captures how tightly a sequence’s token embeddings cluster around the sequence mean.

$$\text{WithinSeqVar} = \mathbf{Ave}_{t,i,c} \|X_{t,i,c} - \mu_{i,c}\|^2.$$

The *within-class variance* captures how much sequence means vary across examples from the same class:

$$\text{WithinClassVar} = \mathbf{Ave}_{i,c} \|\mu_{i,c} - \mu_c\|^2.$$

The *between-class variance* captures how separated the class means are from the global mean:

$$\text{BetweenClassVar} = \mathbf{Ave}_c \|\mu_c - \mu_G\|^2.$$

Finally, the *total variance* quantifies the overall variance of all token embeddings around the global mean:

$$\text{TotalVar} = \mathbf{Ave}_{t,i,c} \|X_{t,i,c} - \mu_G\|^2.$$

4.5. Variance Decomposition

By expanding the squared norm, the total variance decomposes additively into the three components defined earlier:

$$\begin{aligned} \text{TotalVar} = & \text{BetweenClassVar} + \text{WithinClassVar} \\ & + \text{WithinSeqVar}. \end{aligned}$$

Following these definitions, we use the last-layer token embeddings to compute the total variance and its decomposition into WithinSeqVar, WithinClassVar and BetweenClassVar, each reported as a fraction of TotalVar. Figure 4 presents the result for models trained on CIFAR-100. As the number of Laplacian heads k increases, the WithinSeqVar fraction drops sharply, while the BetweenClassVar fraction rises substantially, indicating more within-sequence collapse and stronger separability between classes. For models with fewer Laplacian heads ($k = 0, 3, 6$), WithinClassVar constitutes a much larger portion of the total variance than BetweenClassVar. This gap narrows as more Laplacian heads are added, and the two fractions become nearly equal for large k . Overall, adding more Laplacian heads shifts the total variance towards BetweenClassVar, driving tokens towards a geometry with greater between-class separability, consistent with the PCA visualization. Together with the results in Table 2, the ANOVA decomposition suggests that higher classification accuracy is correlated with a token geometry that better separates classes.

4.6. Layerwise Within-sequence Collapse

We measure the average cosine similarity between all pairs of tokens within the same sequence to better quantify within-sequence collapse.

$$\text{CosSim}(X) = \frac{1}{B} \sum_{b=1}^B \frac{1}{T(T-1)} \sum_{\substack{i,j=1 \\ i \neq j}}^T \frac{\langle X_{b,i}, X_{b,j} \rangle}{\|X_{b,i}\| \|X_{b,j}\|}.$$

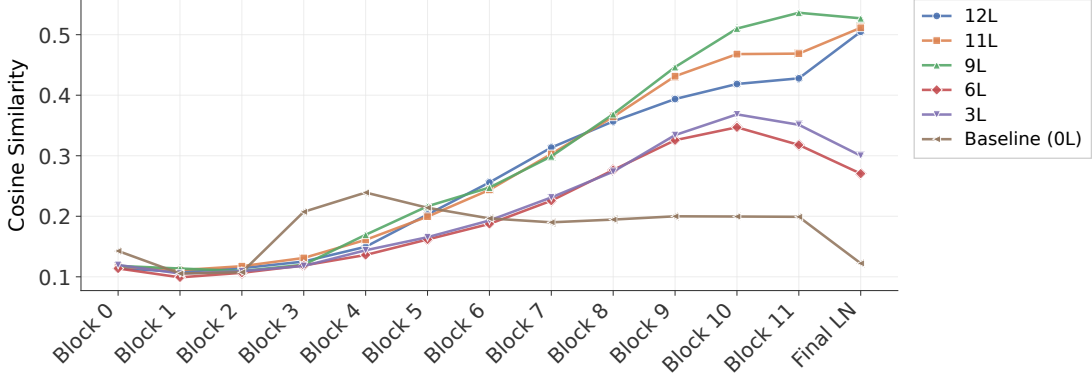


Figure 5. The Laplacian mechanism induces a significantly steeper increase in CosSim across depth. Measured on ImageNet, “L” denotes the number of Laplacian heads.

Here, $X_{b,i} \in \mathbb{R}^d$ denotes the i -th token in the b -th sequence. CosSim lies between -1 and 1 , and a larger value indicates that more within-sequence alignment tokens.

Figure 5 shows CosSim for the output tokens of each transformer block in models trained on ImageNet. For ViT-B, CosSim remains small across all layers, indicating limited within-sequence collapse. As more Laplacian heads are added, we observe a steeper increase in CosSim across depth, reaching higher values towards the end. This behavior suggests that the Laplacian heads induce stronger alignment among tokens in deeper layers.

4.7. Neural Collapse Metrics and Visualization

Finally, we use the Neural Collapse metrics from Han et al. (2022) to assess the geometric configuration of tokens. We also complement these metrics with a visualization technique introduced by Fisher et al. (2024) (Algorithm 2). Full details are provided in Appendix F.

Figure 6 compares the four NC metrics for CIFAR100 models with varying numbers of Laplacian heads. Figures 24a and 24b show that increasing the number of Laplacian heads yields token embeddings that are more equinorm and equiangular, while Figure 24c illustrates stronger duality between token representations and classifier weights. Together, these results indicate that the Laplacian heads promote a simplex ETF structure in both the class means and classifier weights, with the effect strengthening as the number of Laplacian heads increases. Finally, Figure 24d shows that models with more Laplacian heads are significantly closer to a nearest-class-center classifier.

Figure 7 visualizes the token embeddings projected onto the classifier for ViT-B and ViT-B-12L. While the baseline displays diffuse, overlapping clouds of tokens from different classes, ViT-B-12L produces well-separated clusters with a clear simplex-like arrangement, further corroborating the NC2-NC4 metrics. Across all models, the projections also

reveal clearer simplex structure as the number of Laplacian heads increases (see Appendix C.5).

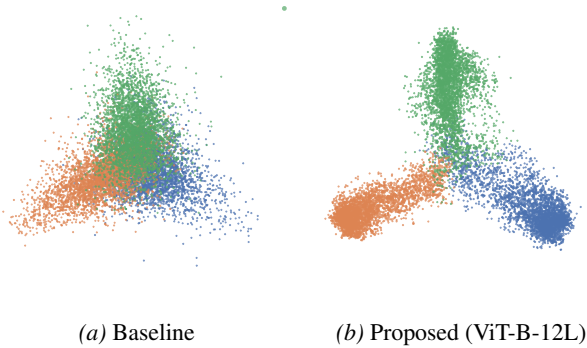


Figure 7. Laplacian heads promote a simplex in token embeddings between classes.

5. Neural Token Collapse: a Geometry of Maximal Separability

Based on our findings in Section 4, we formally define the geometry that emerges in token representations as a result of the Laplacian mechanism. We name this geometry *Neural Token Collapse* (NTC). It is characterized by the following properties:

NTC0 All tokens within a sequence coincide with that sequence’s mean,

$$\forall 1 \leq c \leq C, 1 \leq t \leq T, 1 \leq i \leq N_c, \quad X_{t,i,c} = \mu_{i,c}$$

which implies

$$\text{WithinSeqVar} = 0.$$

NTC1 All sequence means within a class coincide with the class mean,

$$\mu_{i,c} = \mu_c \quad \forall 1 \leq i \leq N_c,$$

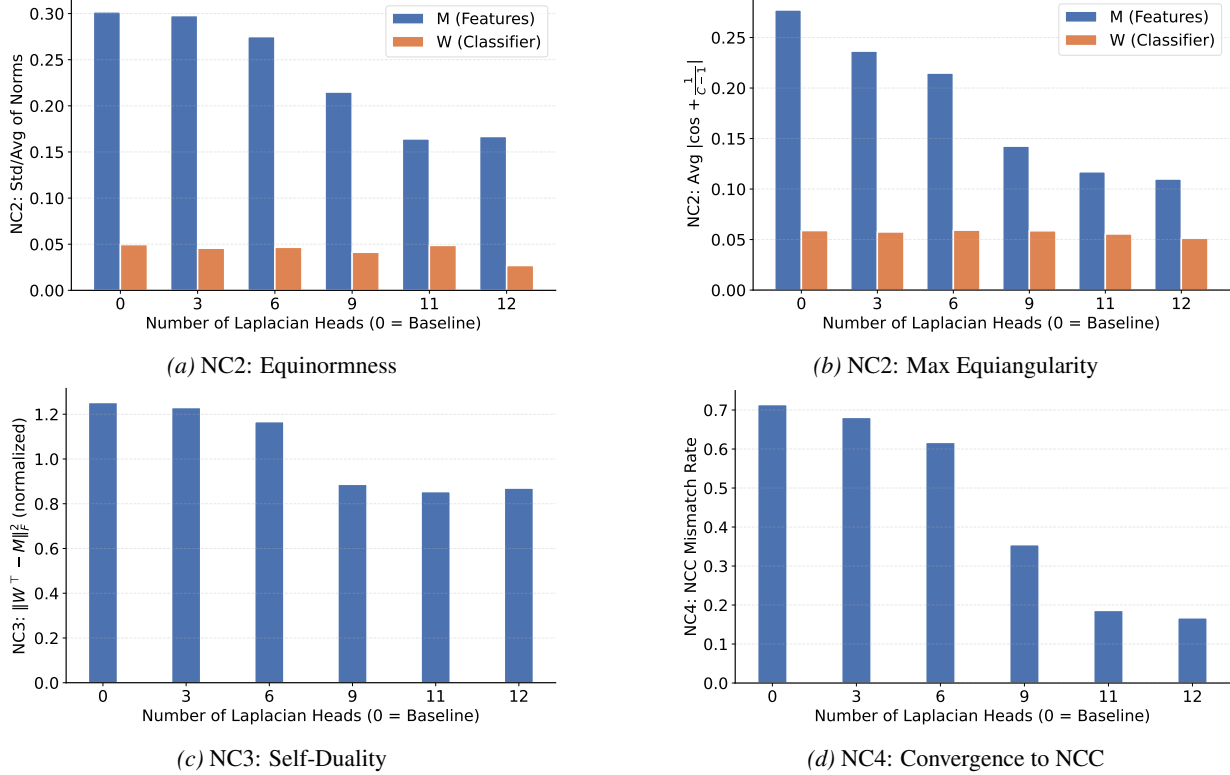


Figure 6. Neural-collapse metrics on CIFAR-100 (a–d). M denotes the matrix of class means—averaged over all tokens and instances within each class—while W denotes the classifier weight matrix.

which implies

$$\text{WithinClassVar} = 0.$$

Combined with NTC0, this further implies

$$\text{TotalVar} = \text{BetweenClassVar}.$$

NTC2-4 The class means

$$\{\mu_c : 1 \leq c \leq C\},$$

together with the classifier weights, satisfy NC2, NC3, and NC4 as defined in (Papyan et al., 2020).

6. Relation to Diffusion Over Graphs

Our Laplacian mechanism can be understood through the lens of diffusion on graphs, in particular the discrete heat equation.

Connection to graphs Consider a sequence of T tokens. Treat each token as a vertex in a graph $G = (V, E)$ with $|V| = T$. The attention weights from (1),

$$P = \text{softmax}\left(\frac{QK^\top}{\sqrt{d_k}}\right) \in \mathbb{R}^{T \times T},$$

define directed edge weights: P_{ij} encodes the normalized influence of token j on token i . Because each row sums to one, P is a row-stochastic adjacency matrix.

The graph Laplacian. Given P , the random-walk normalized graph Laplacian is

$$\mathbf{L} = I - P,$$

where $I \in \mathbb{R}^{T \times T}$ is the identity matrix. Since P is row-stochastic, applying \mathbf{L} to $x \in \mathbb{R}^T$ measures its deviation from the local row-normalized average over neighbors.

Diffusion as the discrete heat equation. Diffusion on a graph evolves $x(t)$ according to

$$\frac{d}{dt}x(t) = -\mathbf{L}x(t),$$

whose solution progressively smooths x along the edges. A single explicit Euler step with step size $\Delta t = 1$ gives

$$x_{t+1} = x_t - \mathbf{L}x_t = x_t - (I - P)x_t.$$

Connecting diffusion to our mechanism. This update matches exactly what our Laplacian head together with the residual connection in (2) performs:

$$X' = X - \mathbf{L}(V) = X - (I - P)V.$$

The residual connection in (2) is written with the opposite sign convention, i.e. $X' = X + \mathbf{L}(V)$. This is purely a notational choice: the sign can always be absorbed into the learnable matrices (for example, replacing W_V by $-W_V$ leaves the mechanism mathematically equivalent).

Consequences for token geometry. Repeated application of the normalized graph Laplacian derived from attention scores drives token representations toward their locally averaged state, reducing within-sequence variance and moving them closer to the geometry described in Subsection 5.

7. Related Works

Neural Collapse NC is a set of phenomena describing the training dynamics of deep classifiers in the terminal phase (Papyan et al., 2020). It reveals the emergence of a distinctive geometry in the final-layer representations. NC has been widely studied in various settings (Han et al., 2022; Zhu et al., 2021; Zhou et al., 2022a;b; Rangamani et al., 2023; Jacot et al., 2024; Wu & Papyan, 2024; Fisher et al., 2024; Yan et al., 2024). Recent work by Súkeník et al. (2025) shows that NC is optimal for transformers and ResNet, and several works focus on inducing NC-related properties in the last-layer features and weights (Markou et al., 2024; Chen et al., 2024). However, these works do not study within-sequence variance of tokens. Many other works leverage the properties of NC to perform specific tasks (Ammar et al., 2024; Pham et al., 2025).

Rank Collapse *rank collapse* is the phenomenon where the dimension of token embeddings progressively decreases as they pass through transformer blocks (Dong et al., 2023; Noci et al., 2022; Saada et al., 2025; Geshkovski et al., 2025; Kirsanov et al., 2025; Zhou et al., 2025; Bruno et al., 2025). It is commonly regarded as a degeneracy because it can hinder optimization (Noci et al., 2022) and reduce expressivity (Dong et al., 2023; Barbero et al., 2024). Our work shows that tokens could collapse into a specific geometry that is beneficial for classification, so collapse is not universally bad. Relatedly, Geshkovski et al. (2024) characterize the limiting geometries emerging from self-attention dynamics but do not connect them to performance. Viswanathan et al. (2025) measure some geometric properties of token embeddings in large language models. They find that higher-loss prompts yield embeddings with higher intrinsic dimension, also pointing to the potential value of controlled collapse.

Token Collapse in Autoregressive Language Models A recent work by (Zhang et al., 2025) observes a low-rank structure in the token embeddings of transformers trained for next-token prediction. More explicitly, (Zhao et al., 2025) show that next-token prediction implicitly favors learning logits with a sparse-plus-low-rank structure, where

the low-rank component becomes dominant during training and depends only on the support pattern of the context–token co-occurrence matrix. Consequently, when projected onto an appropriate subspace, contexts that share similar next-token supports collapse toward shared low-dimensional directions—a phenomenon they term *subspace collapse*. Our results in Section 3.2 are consistent with their theories: the Laplacian heads could induce subspace collapse more efficiently, leading to improved downstream performance.

Oversmoothing in Graph Neural Networks Since transformers can be viewed as graph neural networks (GNNs) (Joshi, 2025), our work is related to the oversmoothing phenomenon in GNNs (Roth & Liebig, 2024; Rusch et al., 2023; Álvaro Arroyo et al., 2025). Like rank collapse, oversmoothing is regarded as an issue to be mitigated (Roth et al., 2024; Rusch et al., 2022; Nguyen et al., 2023; Bodnar et al., 2023; Wang et al., 2022). In particular, (Rusch et al., 2022) addresses oversmoothing by modifying the underlying GNN dynamics. From this perspective, our modification can be understood as discrete heat diffusion on graphs, a connection that we discuss in Section 6.

8. Conclusion

The ability to regulate the variance of token representations is crucial for transformers to attain the optimal geometry. Standard transformers control variance indirectly by updating the mean of token embeddings and applying normalization. We proposed the Laplacian mechanism that allows transformers to increase or decrease token variance more directly via the residual connection. We showed empirically that the Laplacian mechanism improves transformers on various datasets. Further, we established a correlation between the improvements on classification tasks and the emergence of Neural Token Collapse, a geometry whose simplex structure admits maximal separability between classes. Our work proposes a simple and parameter-free modification that improves transformers, and it reveals insights on what might be the ideal geometry for transformer classifiers.

Our investigation of token geometry focused on supervised classification tasks. It is important to note that self-supervised learning (SSL) objectives constitute fundamentally different settings. While we expect the direct control over token variance afforded by Laplacian heads to be beneficial (and indeed we saw improvements on next-token prediction), further work is needed to understand the underlying mechanism. Neural Token Collapse may not be universally optimal, and some SSL objectives might require token variance to evolve in more nuanced ways. Therefore, a future direction is to characterize the optimal geometries for SSL tasks and study whether the Laplacian mechanism can steer token representations towards those ideals.

References

Allal, L. B., Lozhkov, A., Bakouch, E., Blázquez, G. M., Penedo, G., Tunstall, L., Marafioti, A., Kydlíček, H., Lajarín, A. P., Srivastav, V., Lochner, J., Fahlgren, C., Nguyen, X.-S., Fourrier, C., Burtenshaw, B., Larcher, H., Zhao, H., Zakka, C., Morlon, M., Raffel, C., von Werra, L., and Wolf, T. Smollm2: When smol goes big – data-centric training of a small language model, 2025. URL <https://arxiv.org/abs/2502.02737>.

Ammar, M. B., Belkhir, N., Popescu, S., Manzanera, A., and Franchi, G. Neco: Neural collapse based out-of-distribution detection, 2024. URL <https://arxiv.org/abs/2310.06823>.

Ba, J. L., Kiros, J. R., and Hinton, G. E. Layer normalization, 2016. URL <https://arxiv.org/abs/1607.06450>.

Barbero, F., Banino, A., Kapiturowski, S., Kumaran, D., Araújo, J. G. M., Vitvitskyi, A., Pascanu, R., and Veličković, P. Transformers need glasses! information over-squashing in language tasks, 2024. URL <https://arxiv.org/abs/2406.04267>.

Bodnar, C., Giovanni, F. D., Chamberlain, B. P., Liò, P., and Bronstein, M. M. Neural sheaf diffusion: A topological perspective on heterophily and oversmoothing in gnns, 2023. URL <https://arxiv.org/abs/2202.04579>.

Bruno, G., Pasqualotto, F., and Agazzi, A. Emergence of meta-stable clustering in mean-field transformer models, 2025. URL <https://arxiv.org/abs/2410.23228>.

Chen, M., Tworek, J., Jun, H., Yuan, Q., de Oliveira Pinto, H. P., Kaplan, J., Edwards, H., Burda, Y., Joseph, N., Brockman, G., Ray, A., Puri, R., Krueger, G., Petrov, M., Khlaaf, H., Sastry, G., Mishkin, P., Chan, B., Gray, S., Ryder, N., Pavlov, M., Power, A., Kaiser, L., Bavarian, M., Winter, C., Tillet, P., Such, F. P., Cummings, D., Plappert, M., Chantzis, F., Barnes, E., Herbert-Voss, A., Guss, W. H., Nichol, A., Paino, A., Tezak, N., Tang, J., Babuschkin, I., Balaji, S., Jain, S., Saunders, W., Hesse, C., Carr, A. N., Leike, J., Achiam, J., Misra, V., Morikawa, E., Radford, A., Knight, M., Brundage, M., Murati, M., Mayer, K., Welinder, P., McGrew, B., Amodei, D., McCandlish, S., Sutskever, I., and Zaremba, W. Evaluating large language models trained on code, 2021. URL <https://arxiv.org/abs/2107.03374>.

Chen, Z., Zhang, M., Cui, S., Li, H., Niu, G., Gong, M., Zhang, C., and Zhang, K. Neural collapse inspired feature alignment for out-of-distribution generalization. In *The Thirty-eighth Annual Conference on Neural Information Processing Systems*, 2024. URL <https://openreview.net/forum?id=wQpNG9JnPK>.

Clark, P., Cowhey, I., Etzioni, O., Khot, T., Sabharwal, A., Schoenick, C., and Tafjord, O. Think you have solved question answering? try arc, the ai2 reasoning challenge, 2018. URL <https://arxiv.org/abs/1803.05457>.

Cobbe, K., Kosaraju, V., Bavarian, M., Chen, M., Jun, H., Kaiser, L., Plappert, M., Tworek, J., Hilton, J., Nakano, R., Hesse, C., and Schulman, J. Training verifiers to solve math word problems, 2021. URL <https://arxiv.org/abs/2110.14168>.

Cubuk, E. D., Zoph, B., Shlens, J., and Le, Q. V. Randaugment: Practical automated data augmentation with a reduced search space, 2019. URL <https://arxiv.org/abs/1909.13719>.

Deng, J., Dong, W., Socher, R., Li, L.-J., Li, K., and Fei-Fei, L. Imagenet: A large-scale hierarchical image database. In *2009 IEEE Conference on Computer Vision and Pattern Recognition*, pp. 248–255. IEEE, 2009.

Dong, Y., Cordonnier, J.-B., and Loukas, A. Attention is not all you need: Pure attention loses rank doubly exponentially with depth, 2023. URL <https://arxiv.org/abs/2103.03404>.

Fisher, Q., Meng, H., and Popyan, V. Pushing boundaries: Mixup’s influence on neural collapse, 2024. URL <https://arxiv.org/abs/2402.06171>.

Geshkovski, B., Letrouit, C., Polyanskiy, Y., and Rigollet, P. The emergence of clusters in self-attention dynamics, 2024. URL <https://arxiv.org/abs/2305.05465>.

Geshkovski, B., Letrouit, C., Polyanskiy, Y., and Rigollet, P. A mathematical perspective on transformers, 2025. URL <https://arxiv.org/abs/2312.10794>.

Han, X. Y., Popyan, V., and Donoho, D. L. Neural collapse under mse loss: Proximity to and dynamics on the central path, 2022. URL <https://arxiv.org/abs/2106.02073>.

He, K., Zhang, X., Ren, S., and Sun, J. Deep residual learning for image recognition, 2015. URL <https://arxiv.org/abs/1512.03385>.

Hendrycks, D., Burns, C., Basart, S., Zou, A., Mazeika, M., Song, D., and Steinhardt, J. Measuring massive multitask language understanding, 2021. URL <https://arxiv.org/abs/2009.03300>.

Henry, A., Dachapally, P. R., Pawar, S., and Chen, Y. Query-key normalization for transformers, 2020. URL <https://arxiv.org/abs/2010.04245>.

Huang, G., Sun, Y., Liu, Z., Sedra, D., and Weinberger, K. Deep networks with stochastic depth, 2016. URL <https://arxiv.org/abs/1603.09382>.

Jacot, A., Súkeník, P., Wang, Z., and Mondelli, M. Wide neural networks trained with weight decay provably exhibit neural collapse, 2024. URL <https://arxiv.org/abs/2410.04887>.

Joshi, C. K. Transformers are graph neural networks, 2025. URL <https://arxiv.org/abs/2506.22084>.

Karpathy, A. nanochat: The best chatgpt that \$100 can buy. <https://github.com/karpathy/nanochat>, 2025.

Kir sanov, A., Chou, C.-N., Cho, K., and Chung, S. The geometry of prompting: Unveiling distinct mechanisms of task adaptation in language models, 2025. URL <https://arxiv.org/abs/2502.08009>.

Krizhevsky, A. Learning multiple layers of features from tiny images. Technical report, University of Toronto, 2009. Describes the CIFAR-10 dataset.

Loshchilov, I. and Hutter, F. Decoupled weight decay regularization, 2019. URL <https://arxiv.org/abs/1711.05101>.

Lozhkov, A., Ben Allal, L., von Werra, L., and Wolf, T. Fineweb-edu: the finest collection of educational content, 2024. URL <https://huggingface.co/datasets/HuggingFaceFW/fineweb-edu>.

Markou, E., Ajanthan, T., and Gould, S. Guiding neural collapse: Optimising towards the nearest simplex equiangular tight frame. In *The Thirty-eighth Annual Conference on Neural Information Processing Systems*, 2024. URL <https://openreview.net/forum?id=z4FaPUslma>.

Nguyen, T., Nguyen, T. M., and Baraniuk, R. G. Mitigating over-smoothing in transformers via regularized nonlocal functionals, 2023. URL <https://arxiv.org/abs/2312.00751>.

Noci, L., Anagnostidis, S., Biggio, L., Orvieto, A., Singh, S. P., and Lucchi, A. Signal propagation in transformers: Theoretical perspectives and the role of rank collapse, 2022. URL <https://arxiv.org/abs/2206.03126>.

Nvidia, :, Adler, B., Agarwal, N., Aithal, A., Anh, D. H., Bhattacharya, P., Brundyn, A., Casper, J., Catanzaro, B., Clay, S., Cohen, J., Das, S., Dattagupta, A., Delalleau, O., Derczynski, L., Dong, Y., Egert, D., Evans, E., Ficek, A., Fridman, D., Ghosh, S., Ginsburg, B., Gitman, I., Grzegorzek, T., Hero, R., Huang, J., Jawa, V., Jennings, J., Jhunjhunwala, A., Kamalu, J., Khan, S., Kuchaiev, O., LeGresley, P., Li, H., Liu, J., Liu, Z., Long, E., Maha baleshwar, A. S., Majumdar, S., Maki, J., Martinez, M., de Melo, M. R., Moshkov, I., Narayanan, D., Naren thiran, S., Navarro, J., Nguyen, P., Nitski, O., Noroozi, V., Nutheti, G., Parisien, C., Parmar, J., Patwary, M., Paw elec, K., Ping, W., Prabhumoye, S., Roy, R., Saar, T., Sabavat, V. R. N., Satheesh, S., Scowcroft, J. P., Sewall, J., Shamis, P., Shen, G., Shoeybi, M., Sizer, D., Smelyanskiy, M., Soares, F., Sreedhar, M. N., Su, D., Subramanian, S., Sun, S., Toshniwal, S., Wang, H., Wang, Z., You, J., Zeng, J., Zhang, J., Zhang, J., Zhang, V., Zhang, Y., and Zhu, C. Nemotron-4 340b technical report, 2024. URL <https://arxiv.org/abs/2406.11704>.

Papyan, V., Han, X. Y., and Donoho, D. L. Prevalence of neural collapse during the terminal phase of deep learning training. *Proceedings of the National Academy of Sciences*, 117(40):24652–24663, 2020. doi: 10.1073/pnas.2015509117. URL <https://www.pnas.org/doi/abs/10.1073/pnas.2015509117>.

Pham, D. T., Nguyen, H. D., Quoc, N. M. N., Van, L. N., Viet, S. D., and Nguyen, D. A. Hierarchical neural collapse detection transformer for class incremental object detection, 2025. URL <https://arxiv.org/abs/2506.08562>.

Rangamani, A., Lindegaard, M., Galanti, T., and Poggio, T. A. Feature learning in deep classifiers through intermediate neural collapse. In Krause, A., Brunsell, E., Cho, K., Engelhardt, B., Sabato, S., and Scarlett, J. (eds.), *Proceedings of the 40th International Conference on Machine Learning*, volume 202 of *Proceedings of Machine Learning Research*, pp. 28729–28745. PMLR, 23–29 Jul 2023. URL <https://proceedings.mlr.press/v202/rangamani23a.html>.

Roth, A. and Liebig, T. Rank collapse causes over smoothing and over-correlation in graph neural networks, 2024. URL <https://arxiv.org/abs/2308.16800>.

Roth, A., Bause, F., Kriege, N. M., and Liebig, T. Preventing representational rank collapse in mpnns by splitting the computational graph, 2024. URL <https://arxiv.org/abs/2409.11504>.

Rusch, T. K., Chamberlain, B. P., Rowbottom, J., Mishra, S., and Bronstein, M. M. Graph-coupled oscillator networks, 2022. URL <https://arxiv.org/abs/2202.02296>.

Rusch, T. K., Bronstein, M. M., and Mishra, S. A survey on oversmoothing in graph neural networks, 2023. URL <https://arxiv.org/abs/2303.10993>.

Saada, T. N., Naderi, A., and Tanner, J. Mind the gap: a spectral analysis of rank collapse and signal propagation in attention layers, 2025. URL <https://arxiv.org/abs/2410.07799>.

Su, J., Lu, Y., Pan, S., Murtadha, A., Wen, B., and Liu, Y. Roformer: Enhanced transformer with rotary position embedding, 2023. URL <https://arxiv.org/abs/2104.09864>.

Súkeník, P., Lampert, C. H., and Mondelli, M. Neural collapse is globally optimal in deep regularized resnets and transformers, 2025. URL <https://arxiv.org/abs/2505.15239>.

Team, G., Riviere, M., Pathak, S., Sessa, P. G., Hardin, C., Bhupatiraju, S., Hussenot, L., Mesnard, T., Shahriari, B., Ramé, A., Ferret, J., Liu, P., Tafti, P., Friesen, A., Casbon, M., Ramos, S., Kumar, R., Lan, C. L., Jerome, S., Tsitsulin, A., Vieillard, N., Stanczyk, P., Girgin, S., Momchev, N., Hoffman, M., Thakoor, S., Grill, J.-B., Neyshabur, B., Bachem, O., Walton, A., Severyn, A., Parrish, A., Ahmad, A., Hutchison, A., Abdagic, A., Carl, A., Shen, A., Brock, A., Coenen, A., Laforge, A., Paterson, A., Bastian, B., Piot, B., Wu, B., Royal, B., Chen, C., Kumar, C., Perry, C., Welty, C., Choquette-Choo, C. A., Sinopalnikov, D., Weinberger, D., Vijaykumar, D., Rogozińska, D., Heribison, D., Bandy, E., Wang, E., Noland, E., Moreira, E., Senter, E., Eltyshev, E., Visin, F., Rasskin, G., Wei, G., Cameron, G., Martins, G., Hashemi, H., Klimczak-Plucińska, H., Batra, H., Dhand, H., Nardini, I., Mein, J., Zhou, J., Svensson, J., Stanway, J., Chan, J., Zhou, J. P., Carrasqueira, J., Iljazi, J., Becker, J., Fernandez, J., van Amersfoort, J., Gordon, J., Lipschultz, J., Newlan, J., yeong Ji, J., Mohamed, K., Badola, K., Black, K., Milligan, K., McDonell, K., Nguyen, K., Sodhia, K., Greene, K., Sjoesund, L. L., Usui, L., Sifre, L., Heuermann, L., Lago, L., McNealus, L., Soares, L. B., Kilpatrick, L., Dixon, L., Martins, L., Reid, M., Singh, M., Iverson, M., Görner, M., Velloso, M., Wirth, M., Davidow, M., Miller, M., Rahtz, M., Watson, M., Risdal, M., Kazemi, M., Moynihan, M., Zhang, M., Kahng, M., Park, M., Rahman, M., Khatwani, M., Dao, N., Bardoliwalla, N., Devanathan, N., Dumai, N., Chauhan, N., Wahltinez, O., Botarda, P., Barnes, P., Barham, P., Michel, P., Jin, P., Georgiev, P., Culliton, P., Kuppala, P., Comanescu, R., Merhej, R., Jana, R., Rokni, R. A., Agarwal, R., Mullins, R., Saadat, S., Carthy, S. M., Cogan, S., Perrin, S., Arnold, S. M. R., Krause, S., Dai, S., Garg, S., Sheth, S., Ronstrom, S., Chan, S., Jordan, T., Yu, T., Eccles, T., Hennigan, T., Kociský, T., Doshi, T., Jain, V., Yadav, V., Meshram, V., Dharmadhikari, V., Barkley, W., Wei, W., Ye, W., Han, W., Kwon, W., Xu, X., Shen, Z., Gong, Z., Wei, Z., Cotruta, V., Kirk, P., Rao, A., Giang, M., Peran, L., Warkentin, T., Collins, E., Barral, J., Ghahramani, Z., Hadsell, R., Sculley, D., Banks, J., Dragan, A., Petrov, S., Vinyals, O., Dean, J., Hassabis, D., Kavukcuoglu, K., Farabet, C., Buchatskaya, E., Borgeaud, S., Fiedel, N., Joulin, A., Kenealy, K., Dadashi, R., and Andreev, A. Gemma 2: Improving open language models at a practical size, 2024. URL <https://arxiv.org/abs/2408.00118>.

Touvron, H., Cord, M., and Jegou, H. Deit iii: Revenge of the vit. *arXiv preprint arXiv:2204.07118*, 2022.

Vaswani, A., Shazeer, N., Parmar, N., Uszkoreit, J., Jones, L., Gomez, A. N., Kaiser, L., and Polosukhin, I. Attention is all you need. *Advances in neural information processing systems*, 30, 2017.

Viswanathan, K., Gardinazzi, Y., Panerai, G., Cazzaniga, A., and Biagetti, M. The geometry of tokens in internal representations of large language models, 2025. URL <https://arxiv.org/abs/2501.10573>.

Wang, P., Zheng, W., Chen, T., and Wang, Z. Anti-oversmoothing in deep vision transformers via the fourier domain analysis: From theory to practice, 2022. URL <https://arxiv.org/abs/2203.05962>.

Wu, R. and Papyan, V. Linguistic collapse: Neural collapse in (large) language models, 2024. URL <https://arxiv.org/abs/2405.17767>.

Yan, H., Qian, Y., Peng, F., Luo, J., Zhu, Z., and Li, F. Neural collapse to multiple centers for imbalanced data. In *Advances in Neural Information Processing Systems*, 2024. URL <https://openreview.net/forum?id=unknown>. NeurIPS 2024 poster.

Yang, A., Li, A., Yang, B., Zhang, B., Hui, B., Zheng, B., Yu, B., Gao, C., Huang, C., Lv, C., Zheng, C., Liu, D., Zhou, F., Huang, F., Hu, F., Ge, H., Wei, H., Lin, H., Tang, J., Yang, J., Tu, J., Zhang, J., Yang, J., Yang, J., Zhou, J., Zhou, J., Lin, J., Dang, K., Bao, K., Yang, K., Yu, L., Deng, L., Li, M., Xue, M., Li, M., Zhang, P., Wang, P., Zhu, Q., Men, R., Gao, R., Liu, S., Luo, S., Li, T., Tang, T., Yin, W., Ren, X., Wang, X., Zhang, X., Ren, X., Fan, Y., Su, Y., Zhang, Y., Zhang, Y., Wan, Y., Liu, Y., Wang, Z., Cui, Z., Zhang, Z., Zhou, Z., and Qiu, Z. Qwen3 technical report, 2025. URL <https://arxiv.org/abs/2505.09388>.

You, Y., Li, J., Reddi, S., Hseu, J., Kumar, S., Bhojanapalli, S., Song, X., Demmel, J., Keutzer, K., and Hsieh, C.-J. Large batch optimization for deep learning: Training bert in 76 minutes, 2020. URL <https://arxiv.org/abs/1904.00962>.

Zhang, H., Cisse, M., Dauphin, Y. N., and Lopez-Paz, D. mixup: Beyond empirical risk minimization, 2018. URL <https://arxiv.org/abs/1710.09412>.

Zhang, S., Khan, M., and Popyan, V. Attention sinks: A 'catch, tag, release' mechanism for embeddings, 2025. URL <https://arxiv.org/abs/2502.00919>.

Zhao, Y., Behnia, T., Vakilian, V., and Thrampoulidis, C. Implicit geometry of next-token prediction: From language sparsity patterns to model representations, 2025. URL <https://arxiv.org/abs/2408.15417>.

Zhou, J., Li, X., Ding, T., You, C., Qu, Q., and Zhu, Z. On the optimization landscape of neural collapse under mse loss: Global optimality with unconstrained features, 2022a. URL <https://arxiv.org/abs/2203.01238>.

Zhou, J., You, C., Li, X., Liu, K., Liu, S., Qu, Q., and Zhu, Z. Are all losses created equal: A neural collapse perspective, 2022b. URL <https://arxiv.org/abs/2210.02192>.

Zhou, Y., Dai, S., Cao, Z., Zhang, X., and Xu, J. Length-induced embedding collapse in transformer-based models, 2025. URL <https://openreview.net/forum?id=jgISC1wdYy>.

Zhu, Z., Ding, T., Zhou, J., Li, X., You, C., Sulam, J., and Qu, Q. A geometric analysis of neural collapse with unconstrained features, 2021. URL <https://arxiv.org/abs/2105.02375>.

Álvaro Arroyo, Gravina, A., Gutteridge, B., Barbero, F., Gallicchio, C., Dong, X., Bronstein, M., and Vandergheynst, P. On vanishing gradients, over-smoothing, and over-squashing in gnns: Bridging recurrent and graph learning, 2025. URL <https://arxiv.org/abs/2502.10818>.

A. PCA Visualization Method

Let X be a batch of B sequences of token embeddings, represented as a tensor of shape (B, T, d) , where T is the sequence length and d is the embedding dimension.

Algorithm 1 PCA Projection of Tokens to \mathbb{R}^2

Require: $X \in \mathbb{R}^{B \times T \times d}$

```

1:  $X \leftarrow \text{reshape}(X, [B \cdot T, d])$ 
2:  $\mu \leftarrow \text{mean}(X, \text{axis} = 0)$ 
3:  $U, \Sigma, V^\top \leftarrow \text{SVD}(X - \mu)$ 
4:  $V_2 \leftarrow V[:, 0 : 2]$ 
5: return  $(X - \mu) \cdot V_2$ 

```

B. Experiment Details

B.1. Image Classification

To produce results in Table 2, we trained the ViT-B model from (Touvron et al., 2022). The model consists of 12 blocks, with 12 attention heads in each block, and an embedding dimension of 768. The number of trainable parameters is around 86.6 million. For each dataset, we sweep the peak learning rate over the set $\{4e-5, 3e-4, 5e-4, 3e-3, 4e-3\}$ and weight decay over the set $\{0.01, 0.02, 0.05\}$ and select whichever combination that works the best. Many other hyperparameters (such as the mixup (Zhang et al., 2018) α) were selected following the training recipe detailed in (Touvron et al., 2022). Depending on the dataset, we use RandAugment (Cubuk et al., 2019) or 3-Aug (Touvron et al., 2022) for data augmentation and AdamW (Loshchilov & Hutter, 2019) or LAMB (You et al., 2020) as the optimizer. All models in Table 2 were trained for 300 epochs using 3 random seeds. Full details of our training setup, including the hyperparameters that were eventually selected for the experiments, are provided in Table 3.

	CIFAR-10	CIFAR-100	ImageNet
Loss	Cross Entropy	Cross Entropy	Binary Cross Entropy
Optimizer	AdamW	AdamW	LAMB
AdamW β_1	0.9	0.9	0.9
AdamW β_2	0.99	0.99	0.999
Starting Learning Rate	3e-6	3e-6	1e-3
Peak Learning Rate	3e-4	3e-4	3e-3
Minimum Learning Rate	0	0	1e-6
Weight Decay	0.05	0.05	0.02
Drop Path Rate	0.1	0.1	0.3
Batch Size	512	512	2048
Gradient Clipping	1.0	1.0	1.0
LR Scheduler	Cosine Annealing	Cosine Annealing	Cosine Annealing
Warmup Epochs	5	5	5
Data Augmentation	RandAugment	RandAugment	3-Aug
Mixup α	0.8	0.8	0.8
Mixup Probability	1.0	1.0	1.0
Input Size	32×32	32×32	224×224
Patch Size	4×4	4×4	16×16
Precision	float32	float32	bfloat16

Table 3. Training setup for CIFAR-10, CIFAR-100, and ImageNet with hyper-parameter selection informed by (Touvron et al., 2022).

B.2. Autoregressive Next-token Prediction

The model architecture we used was based on (Karpathy, 2025). The model is a decoder-only transformer similar to GPT-2, with the following architectural modification:

- Query-key normalization (Henry et al., 2020; Yang et al., 2025).
- Rotary positional encodings (Su et al., 2023).
- Squared ReLU activation (Nvidia et al., 2024).
- Untied weights for the first-layer embeddings and the last linear layer.
- Soft logits clipping (Team et al., 2024).

Each transformer model we trained has 561 million parameters, with 20 transformer blocks and 10 heads per block. Each model was first pre-trained on roughly 11.2 billion FineWeb-Edu tokens, then mid-trained and supervised fine-tuned on task-mixture datasets. The dataset for mid-training contains SmolTalk(Allal et al., 2025), MMLU(Hendrycks et al., 2021), GSM8K(Cobbe et al., 2021), and synthetic datasets in Karpathy (2025). The dataset for supervised fine-tuning contains SmolTalk, GSM8K, ARC, and the aforementioned synthetic datasets. We use exactly the same training recipe as Karpathy (2025), with the default hyper-parameters.

C. Additional Experiment Results

This section contains additional measurements and visualizations for metrics used in Section 4.

C.1. PCA Visualizations

For CIFAR100 and ImageNet-1k, we first randomly sample 10 and 3 classes, respectively. Then we sample a batch of 512 images that contain roughly an equal number of images across the selected classes. All PCA visualizations in this section are performed using the output of some layer (usually a block from the later half, or the final normalization layer), with the last plot being the output of the normalization layer before the final-layer linear classifier.

C.1.1. CIFAR10

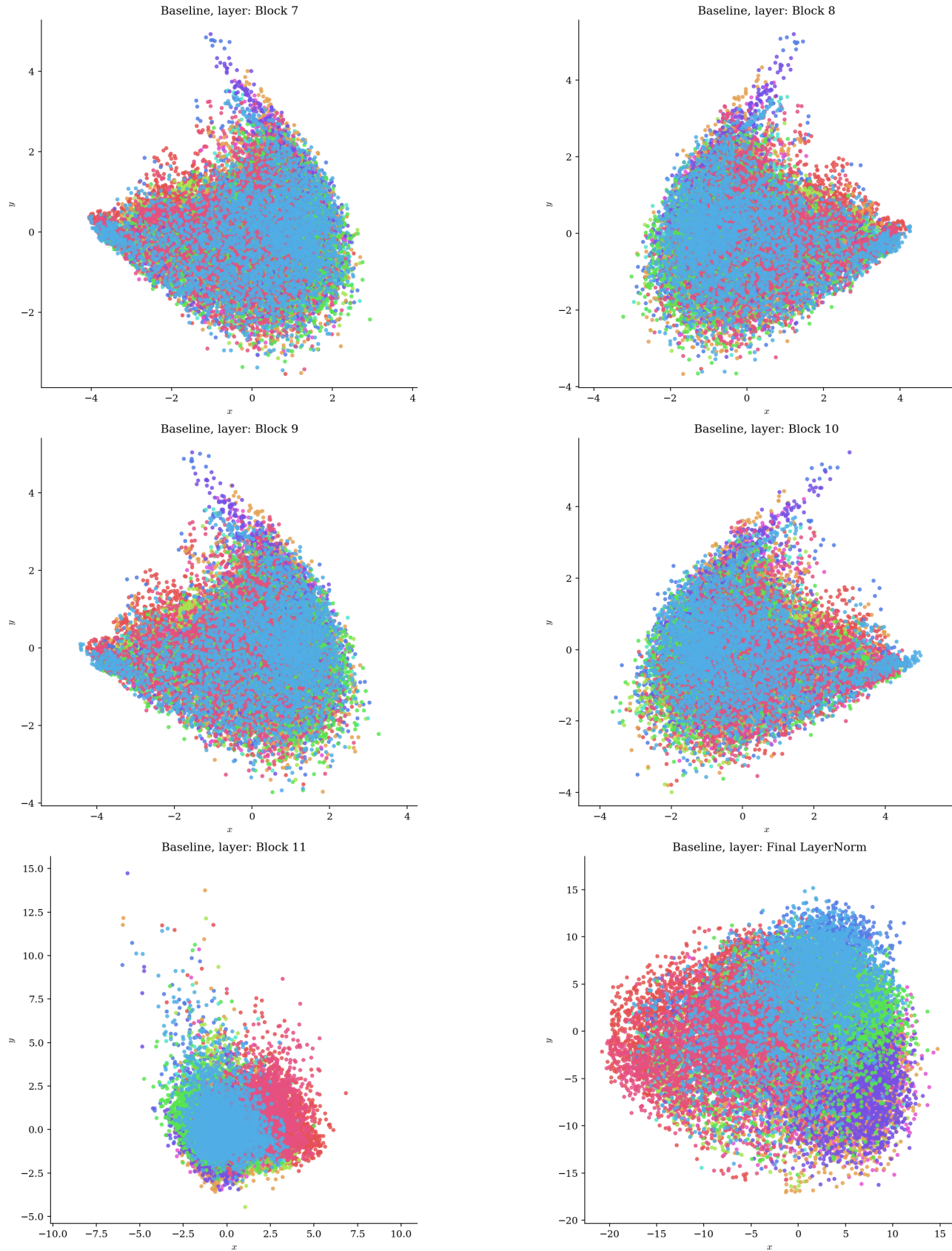


Figure 8. ViT-B (Baseline)

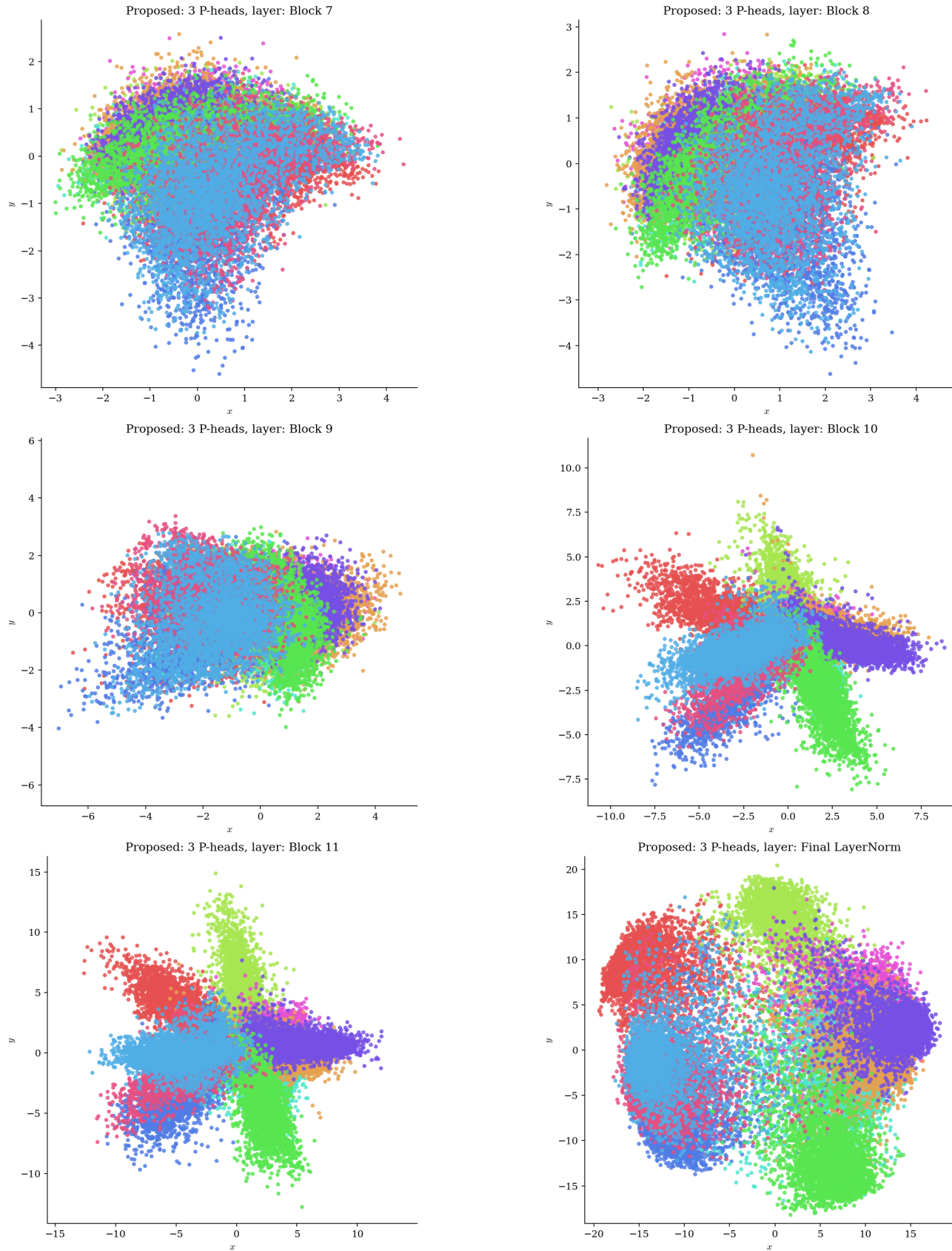


Figure 9. ViT-B-9L (Proposed)

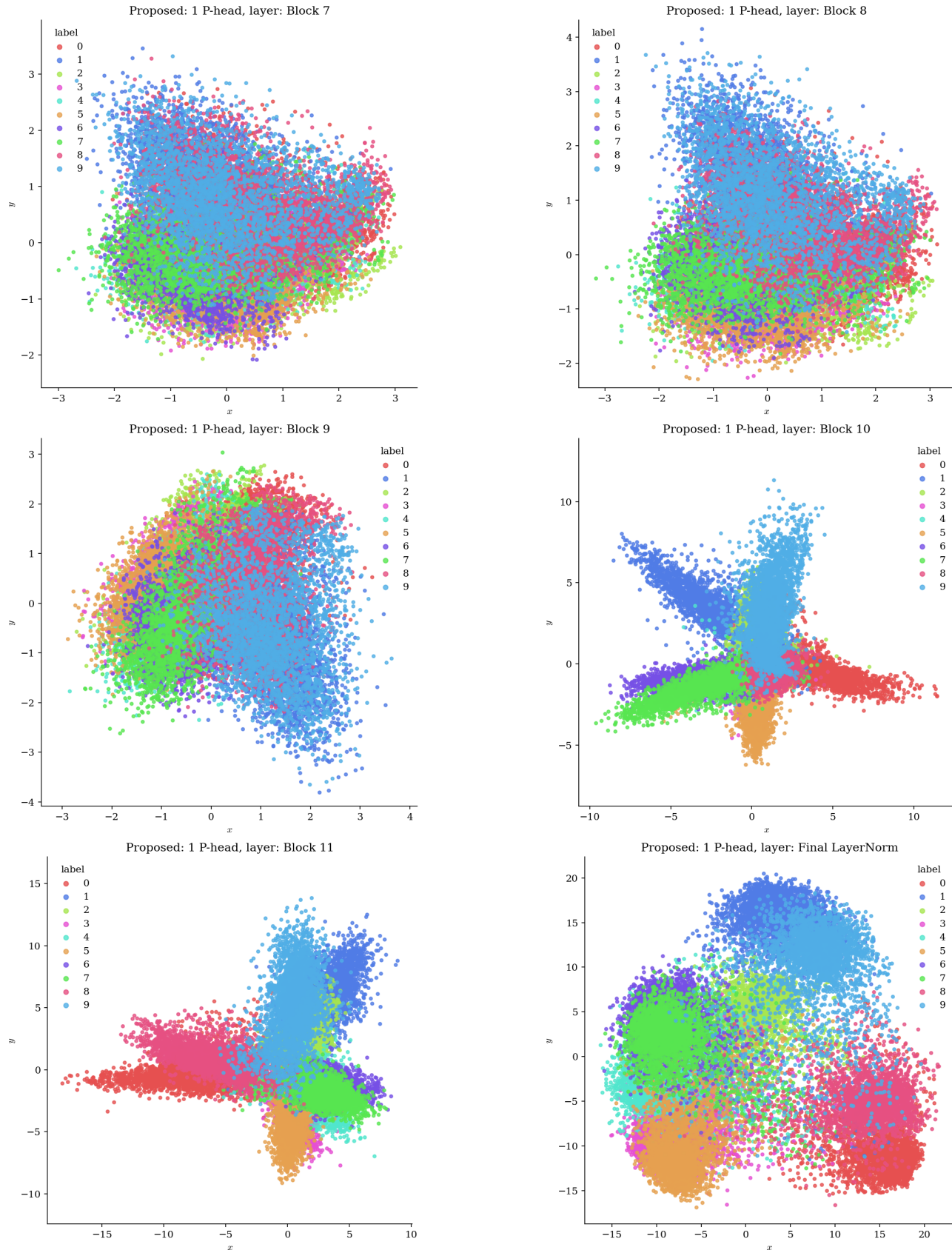


Figure 10. ViT-B-11L (Proposed)

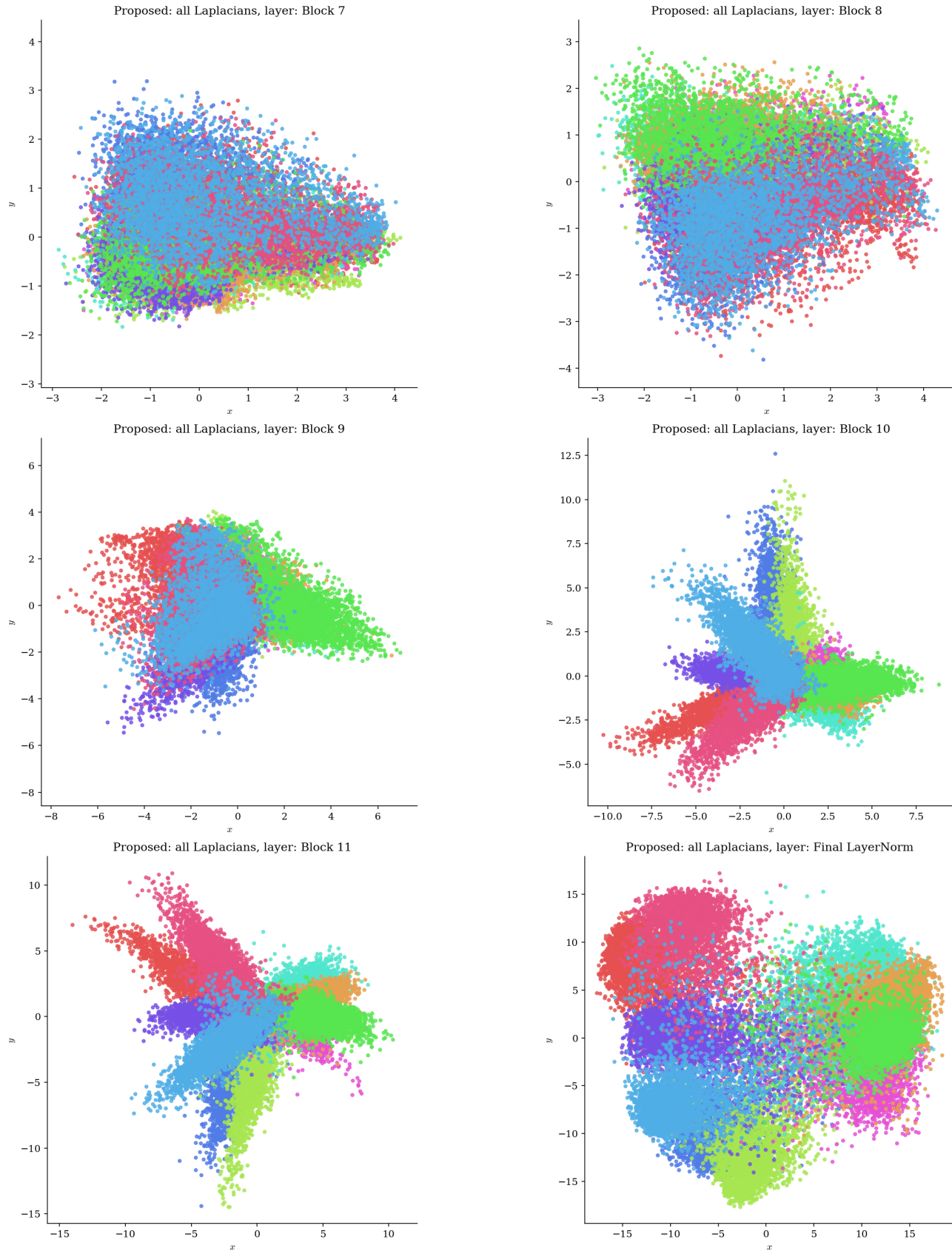


Figure 11. ViT-B-12L (Proposed)

C.1.2. CIFAR100

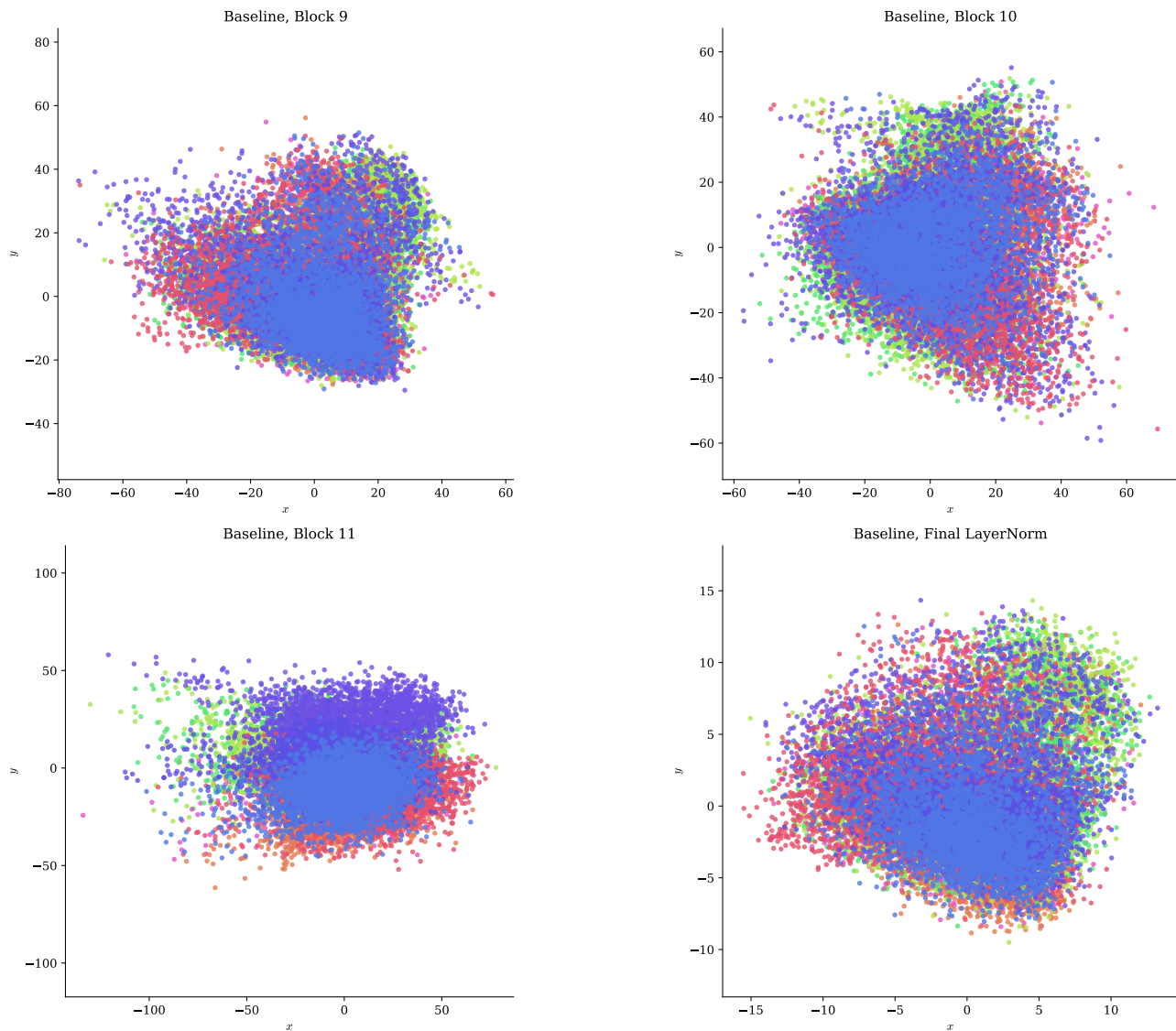


Figure 12. ViT-B (Baseline)

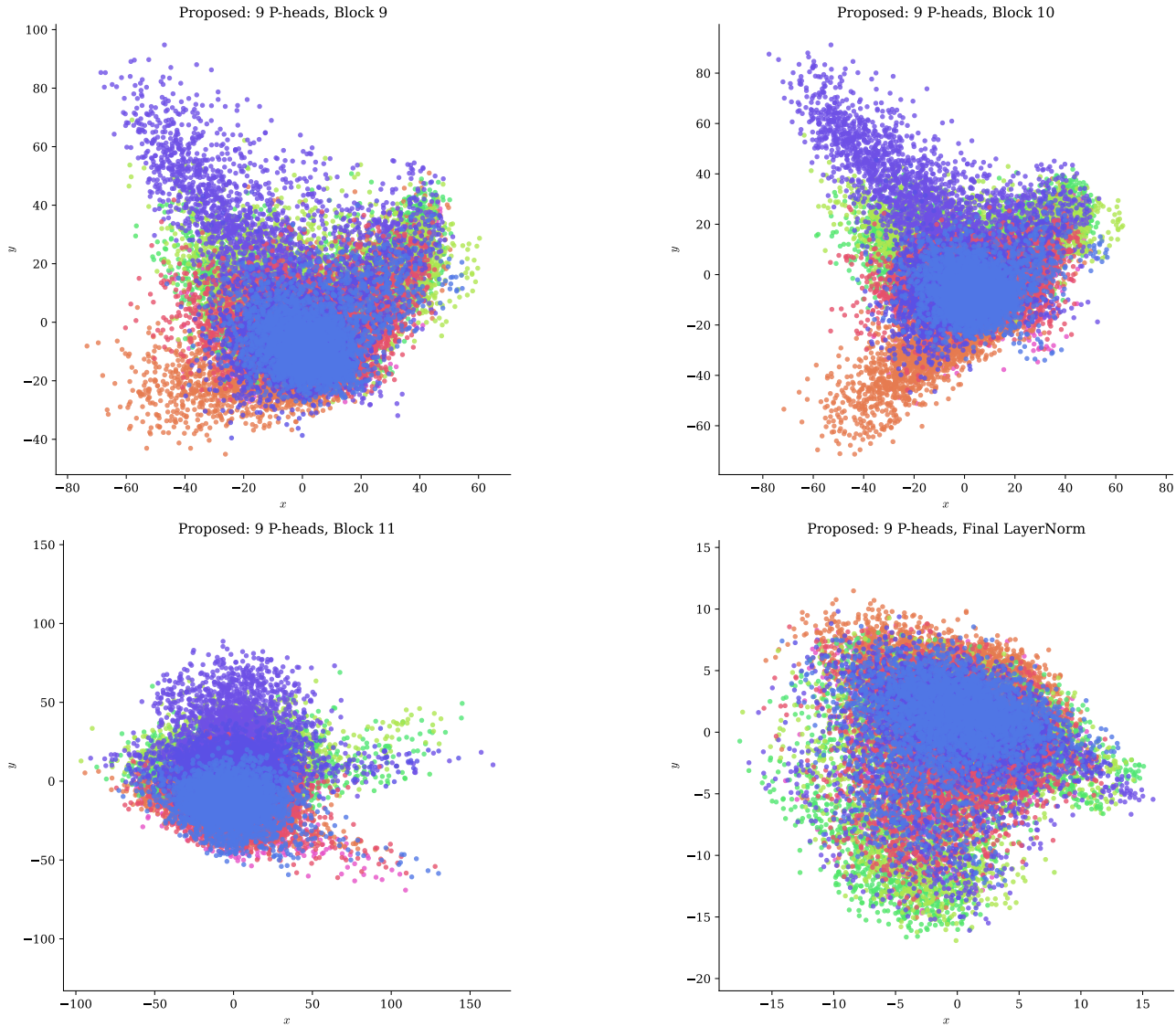


Figure 13. ViT-B-3L (Proposed)

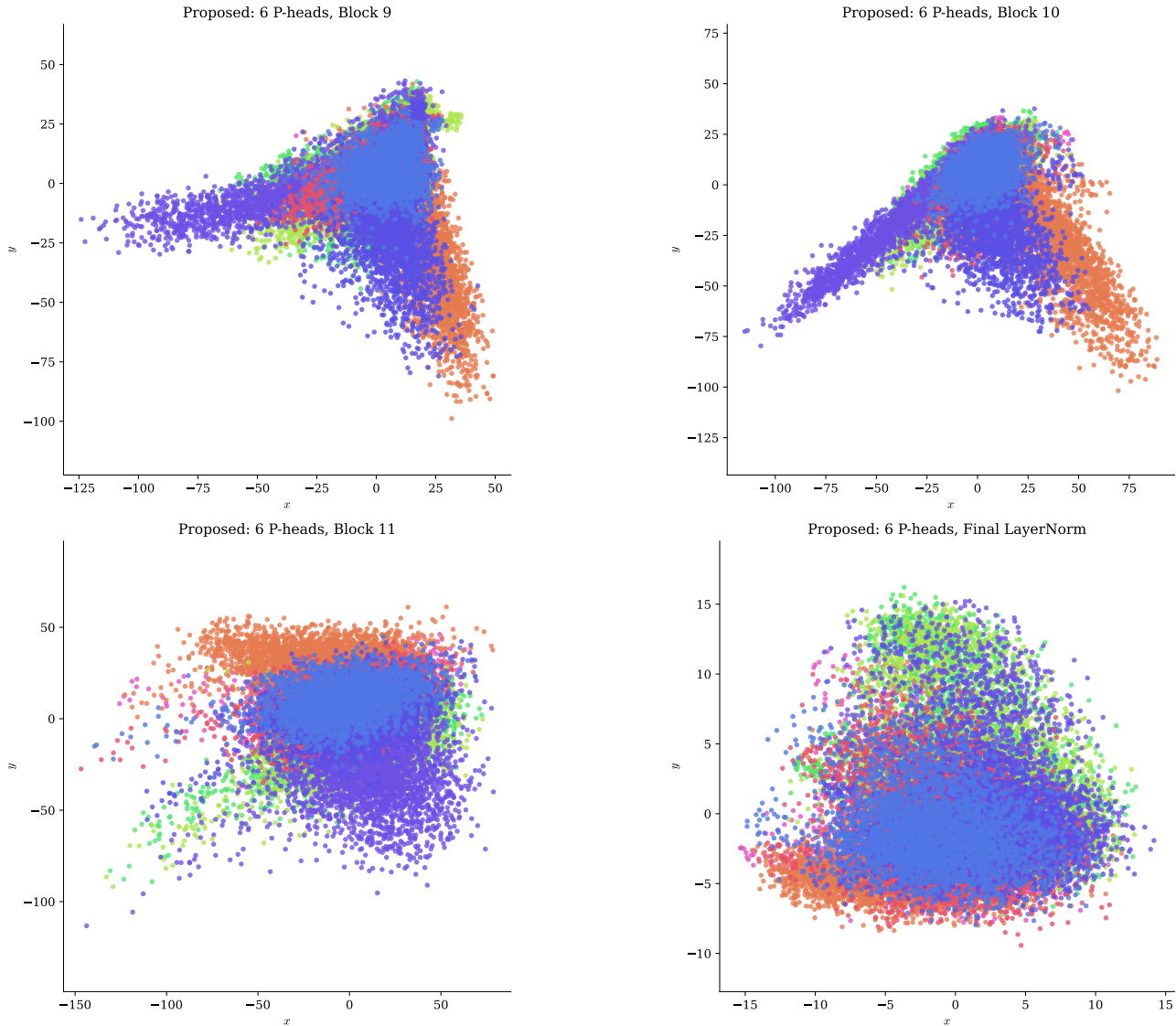


Figure 14. ViT-B-6L (Proposed)

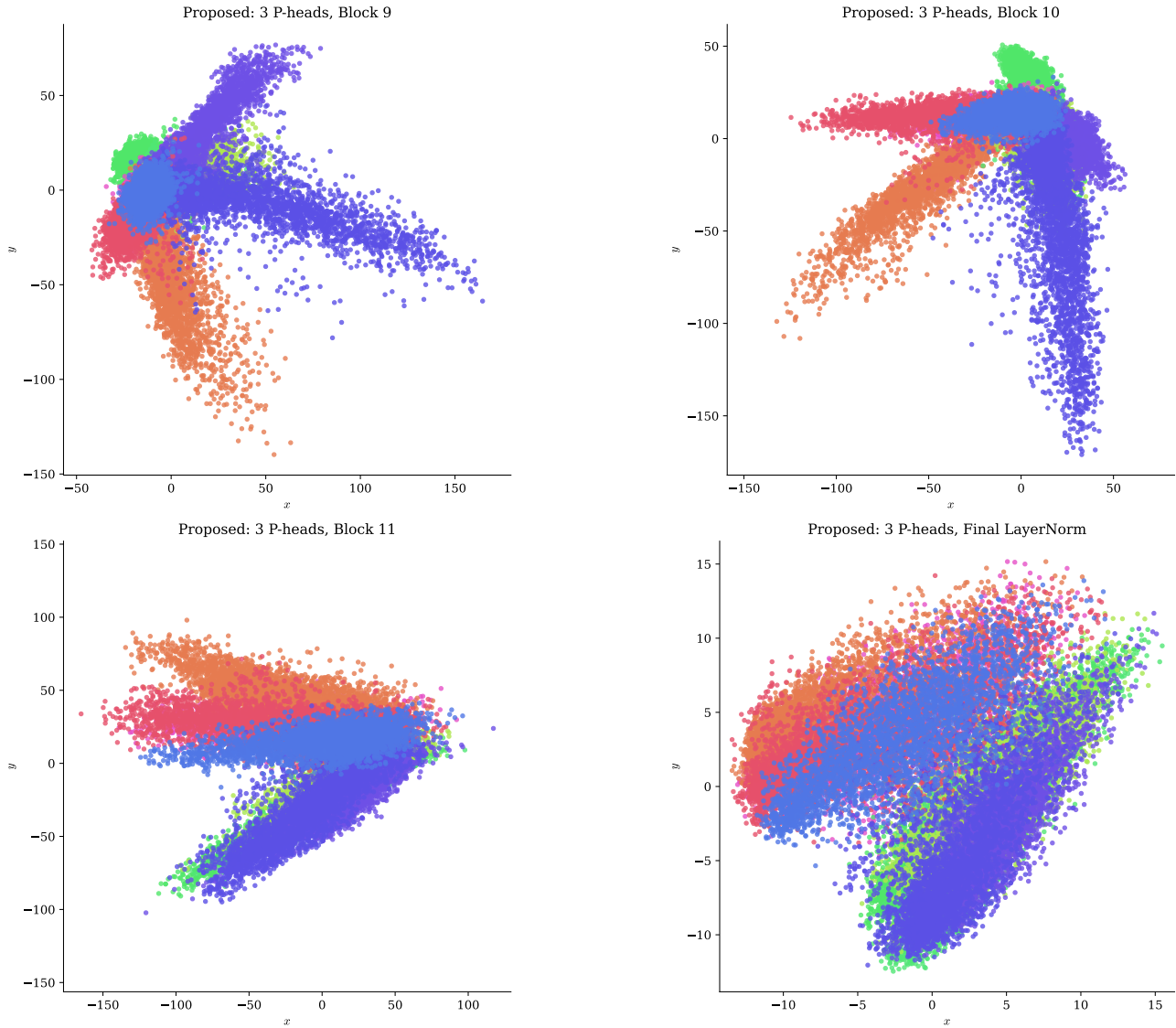


Figure 15. ViT-B-9L (Proposed)

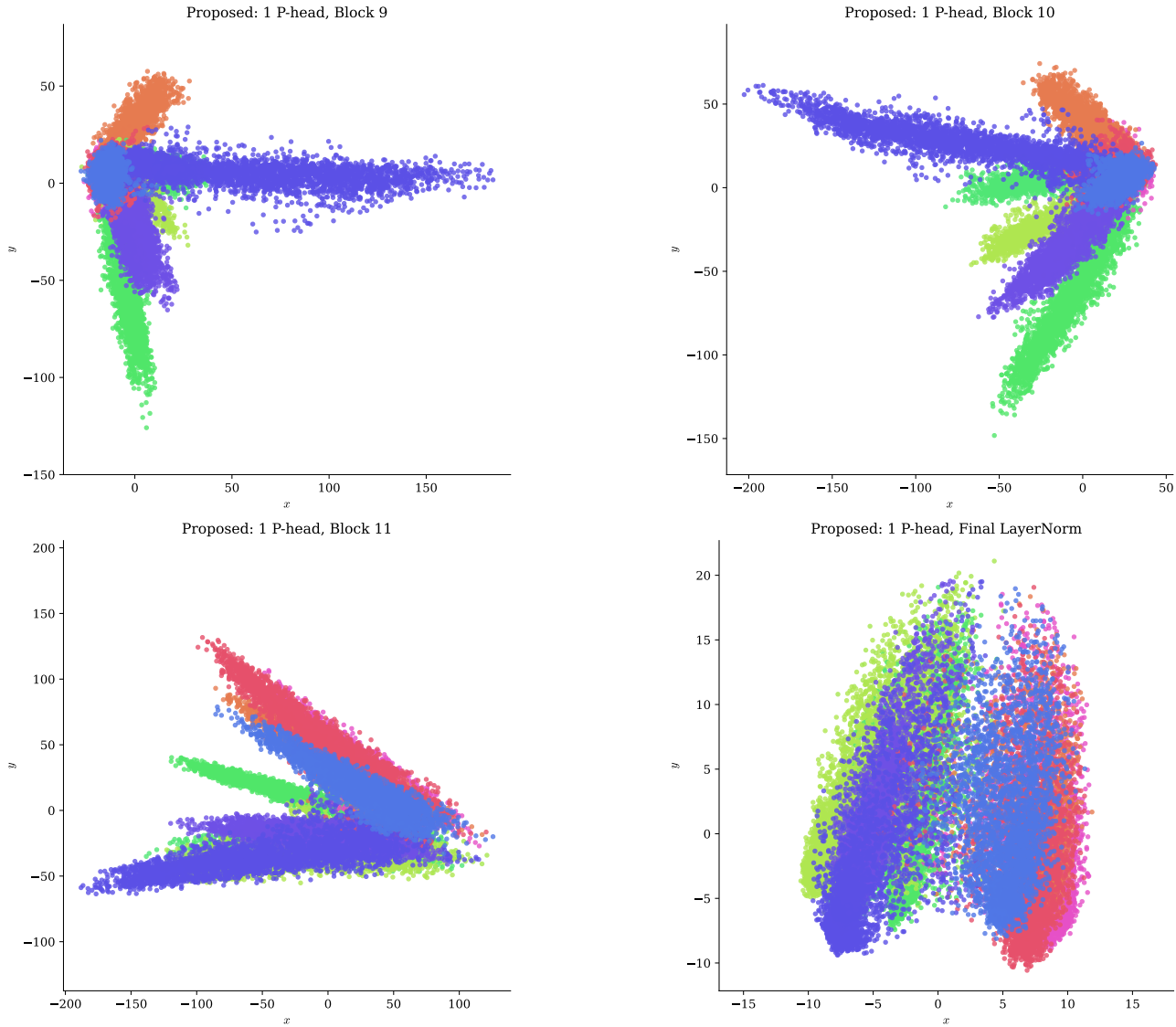


Figure 16. ViT-B-11L (Proposed)

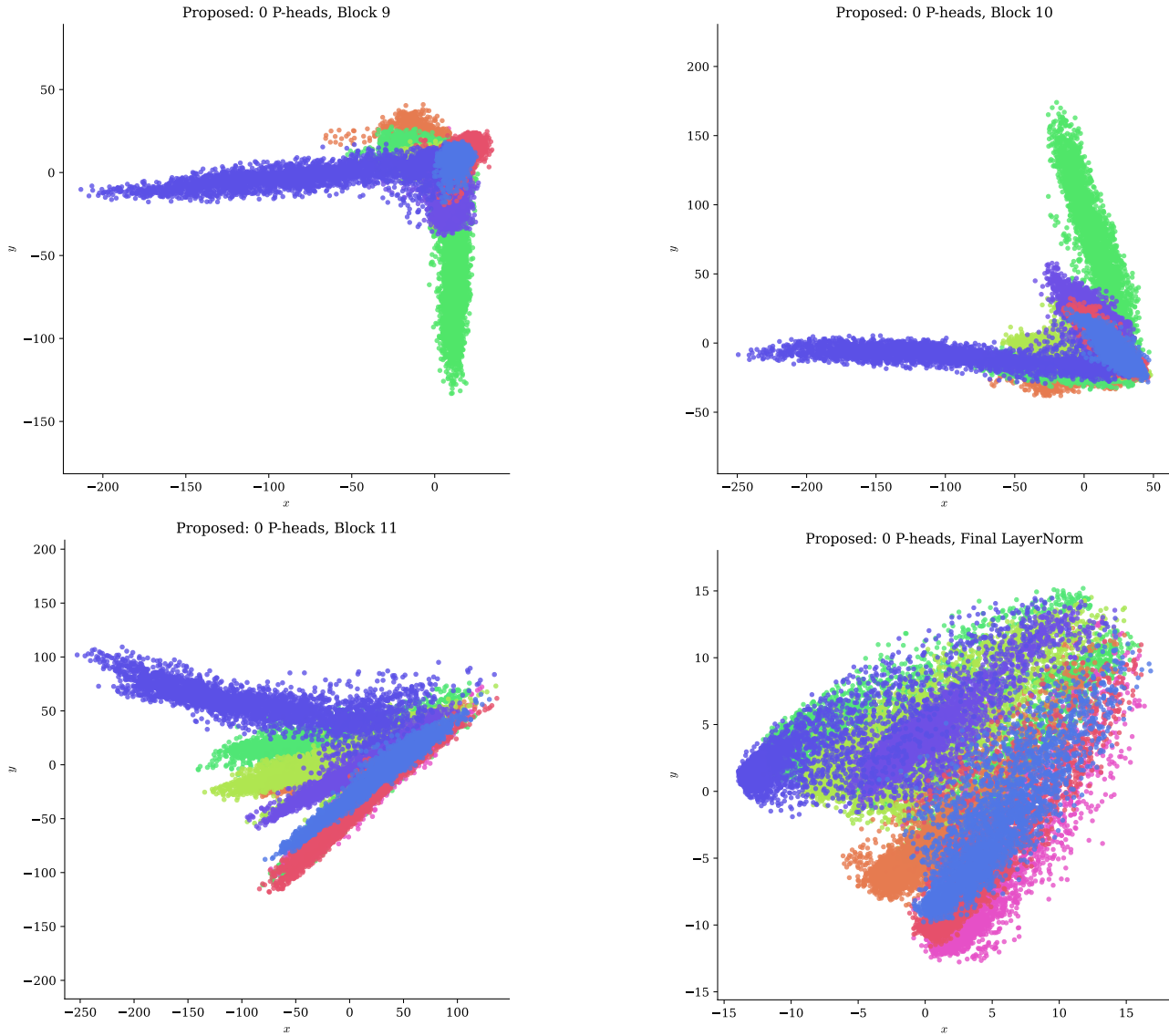


Figure 17. ViT-B-12L (Proposed)

C.1.3. IMAGENET-1K

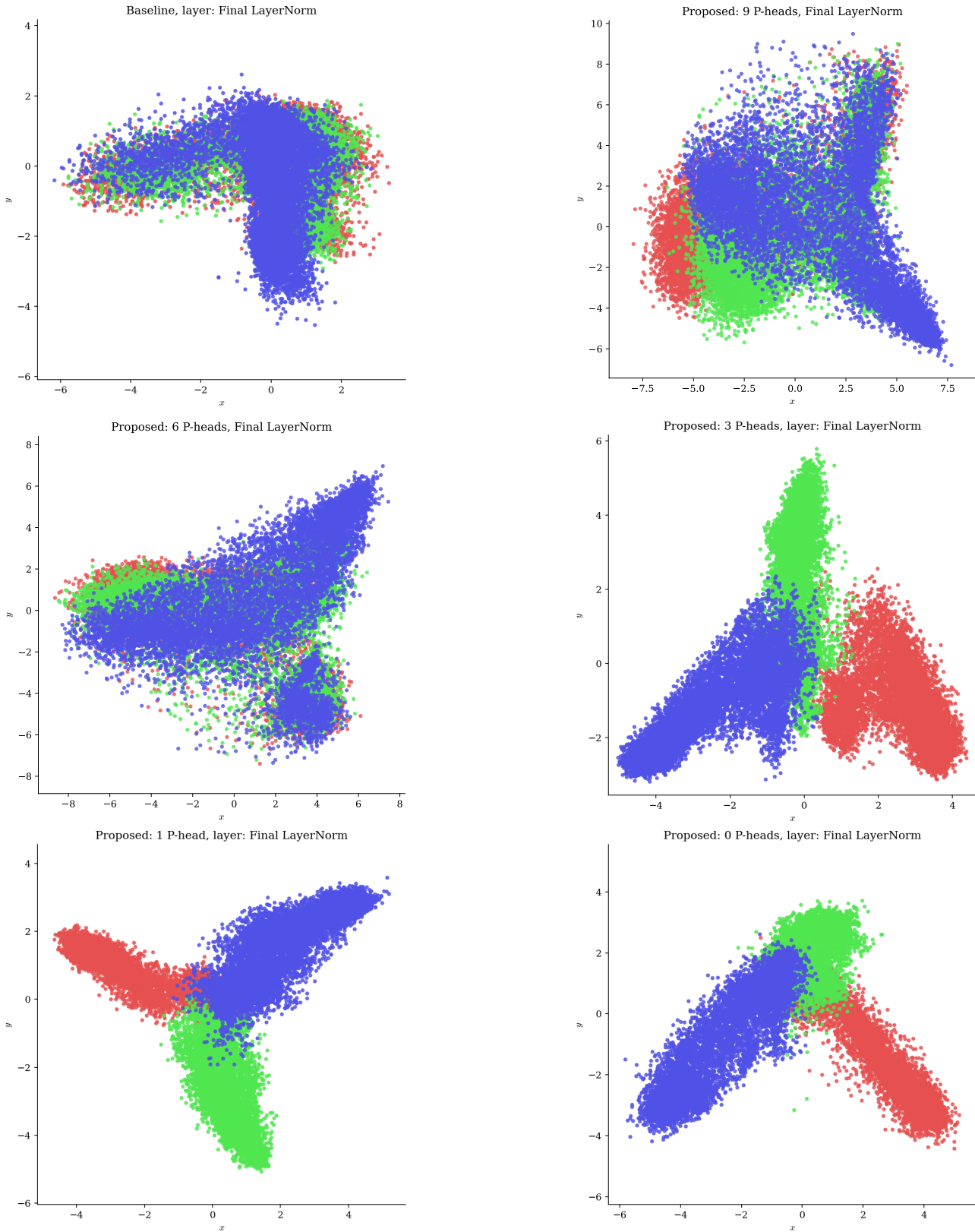


Figure 18. ImageNet-1k PCA projections, as the number of Laplacian heads ranges across $\{0, 3, 6, 9, 11, 12\}$ (from top to bottom, left to right)

C.2. ANOVA decomposition

C.2.1. CIFAR10

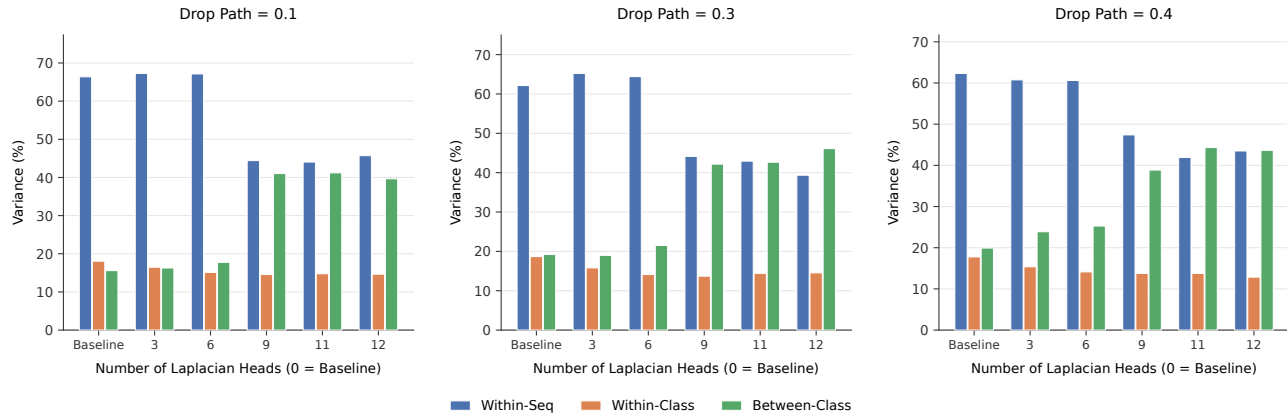


Figure 19. ANOVA decomposition on CIFAR10.

C.2.2. IMAGENET-1K

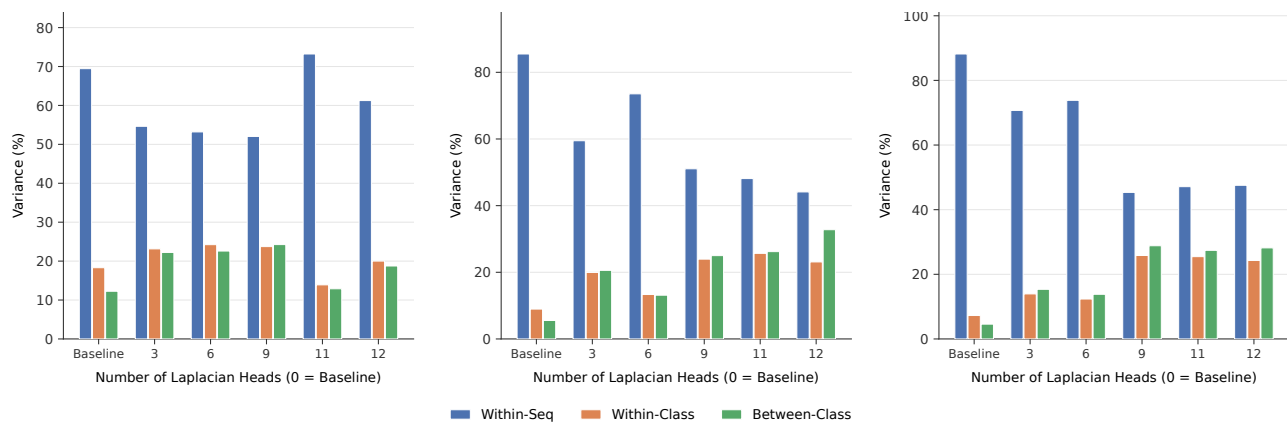


Figure 20. ANOVA decomposition on CIFAR10.

C.3. CosSim Metric

C.3.1. CIFAR10

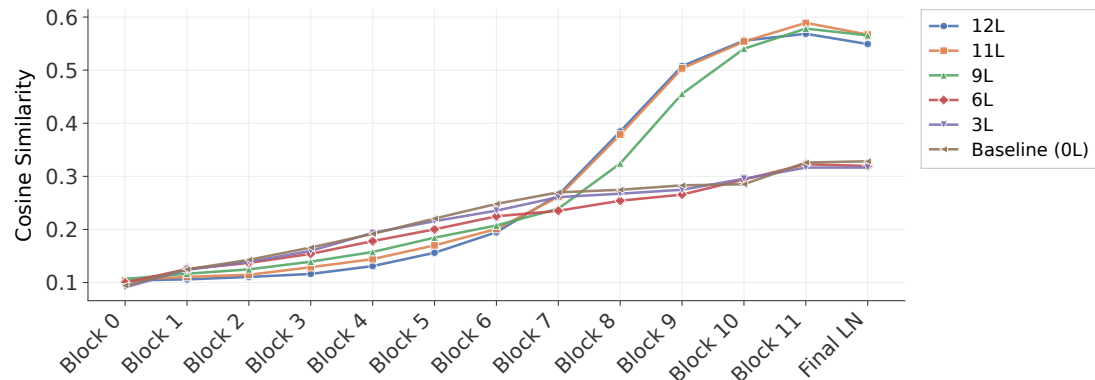


Figure 21. CosSim across depth on CIFAR10.

C.3.2. CIFAR100

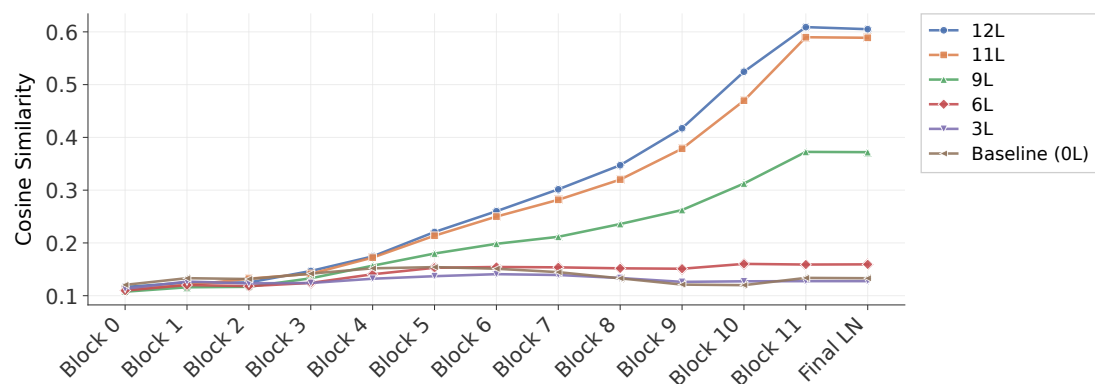


Figure 22. CosSim across depth on CIFAR100.

C.4. NC Metrics and Visualization

C.4.1. CIFAR10

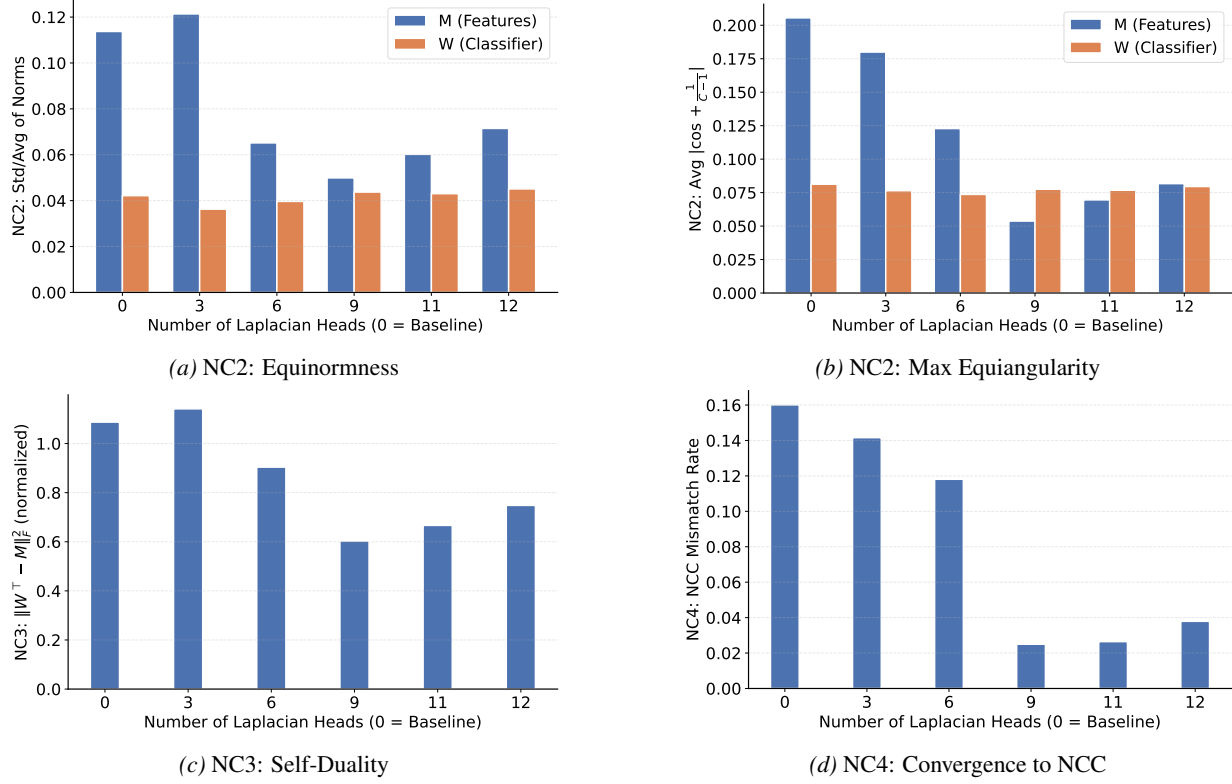


Figure 23. Neural-collapse metrics on CIFAR-10.

C.4.2. IMAGENET-1K

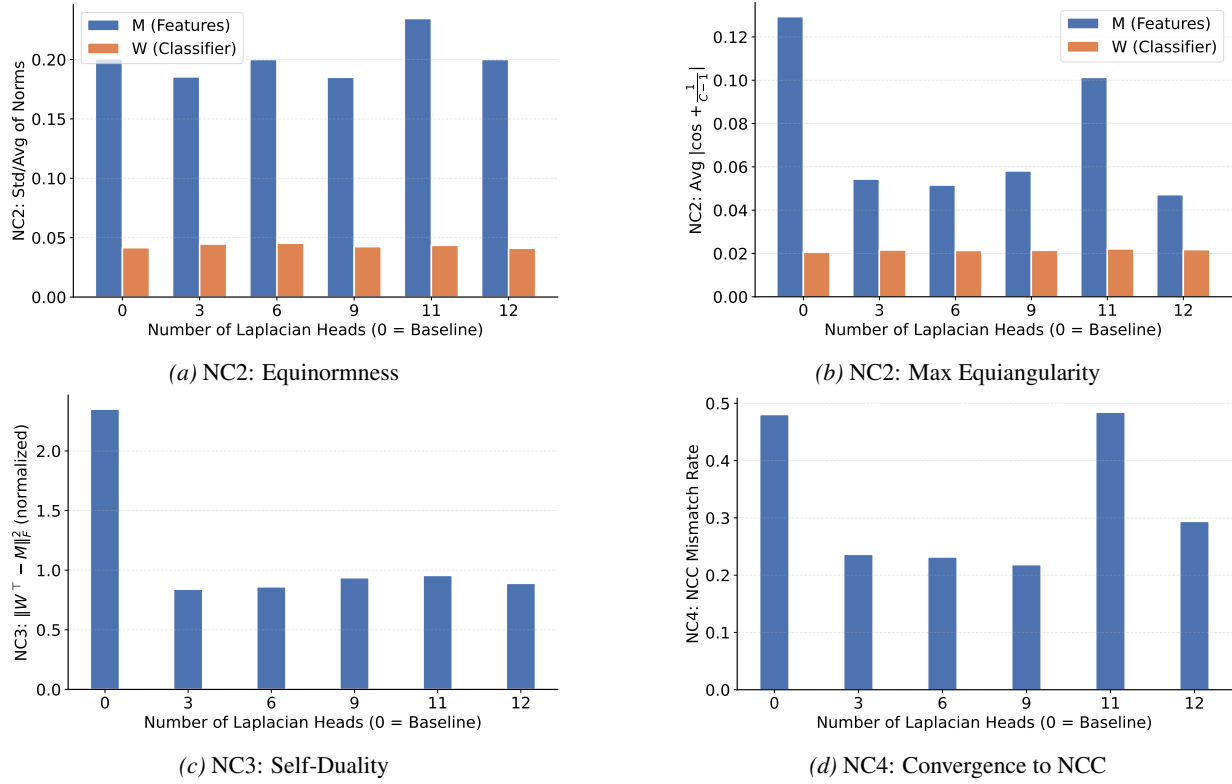


Figure 24. Neural-collapse metrics on ImageNet.

C.5. Visualizations of Projections onto a Simplex

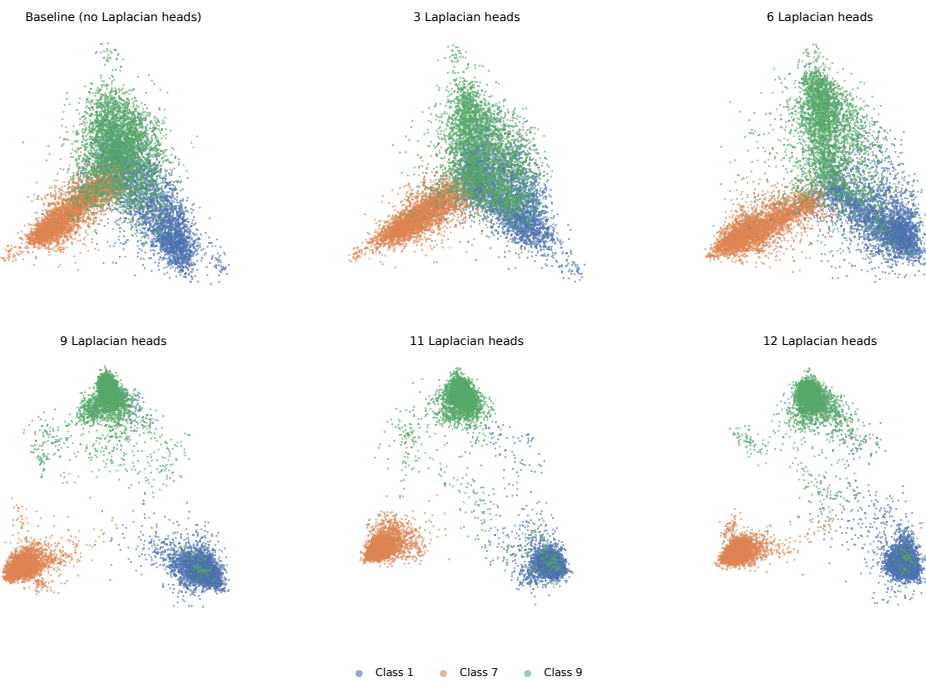


Figure 25. Visualization of Projections on Simplex for CIFAR10

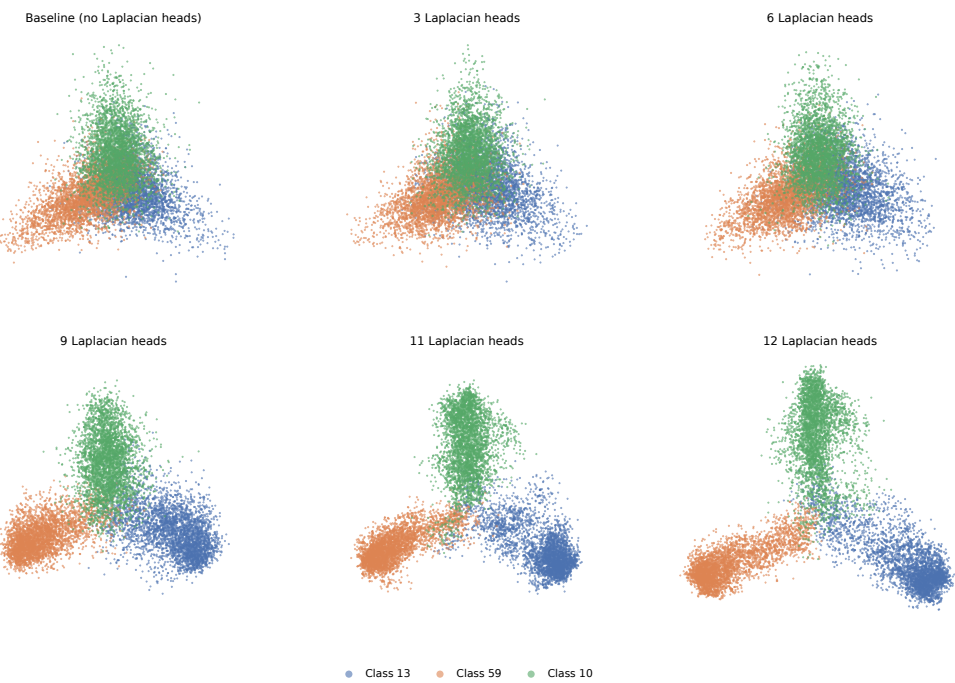


Figure 26. Visualization of Projections on Simplex for CIFAR100

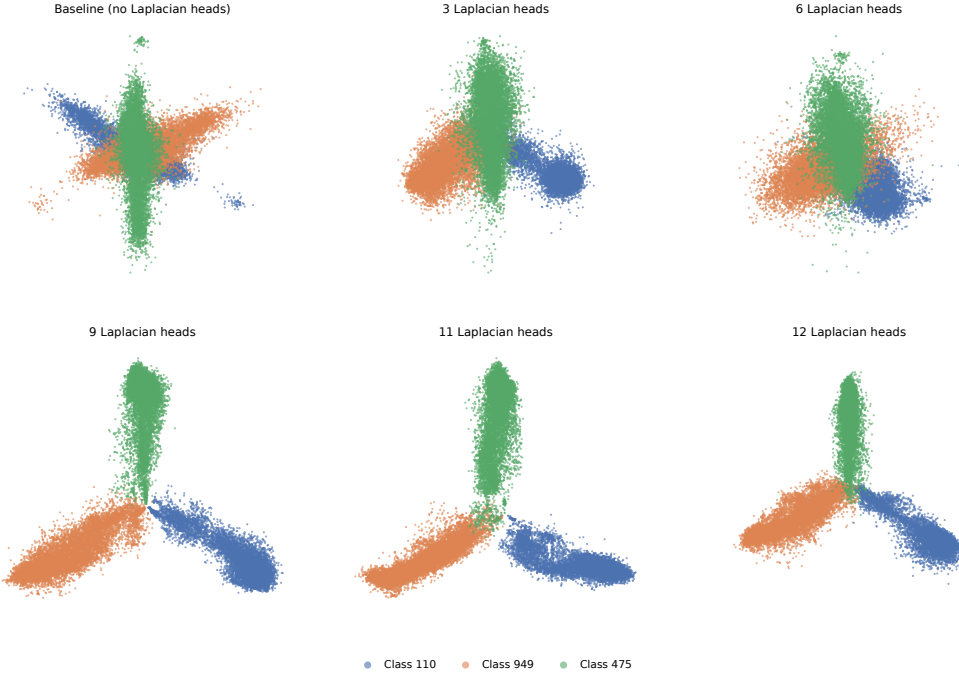


Figure 27. Visualization of Projections on Simplex for ImageNet

D. Empirical Evidence for Geometric Interpretations

Given a batch of sequences of token embeddings $X \in \mathbb{R}^{B \times T \times d}$, we define the average signal-to-noise ratio (SNR) of X as

$$\text{SNR}(X) = \frac{1}{B} \sum_{b=1}^B \frac{\|\text{Mean}(X_b)\|_2}{\text{Std}(X_b)},$$

where

$$\text{Mean}(X_b) = \frac{1}{T} \sum_{i=1}^T X_{b,i} \quad \text{and} \quad \text{Std}(X_b) = \sqrt{\frac{1}{T} \sum_{i=1}^T \|X_{b,i} - \text{Mean}(X_b)\|_2^2}$$

Here, $X_b \in \mathbb{R}^{T \times d}$ denote the b th sequence in the batch and $X_{b,i} \in \mathbb{R}^d$ denote the i th token embedding within the sequence.

The SNR directly measures how large (in l_2 norm) the mean of a sequence of tokens is relative to their variance/standard deviation. To validate our interpretations in Sections 2.1 and 2.2 (see Figure 2), we directly measure the SNR of the output of the Layer Normalization module right before the MLP layer. In other words, we measure the SNR of

$$\text{LayerNorm}(X + \text{MHA}(\text{LayerNorm}(X)))$$

for every transformer block. Figure 28 plots the SNR of the ImageNet token embeddings for the baseline and the proposed models as a function of depth. It clearly illustrates that for all models that use the Laplacian heads, the output of the Pre-MLP LayerNorm has higher SNR than the baseline across layers, growing more drastically as depth increases. Moreover, more Laplacian heads leads to higher SNR and steeper growth. This measurement empirically supports our interpretation of the mechanism by which transformers decrease the variance of tokens, and it directly confirms our intuition that the Laplacian mechanism decreases token variance more efficiently.

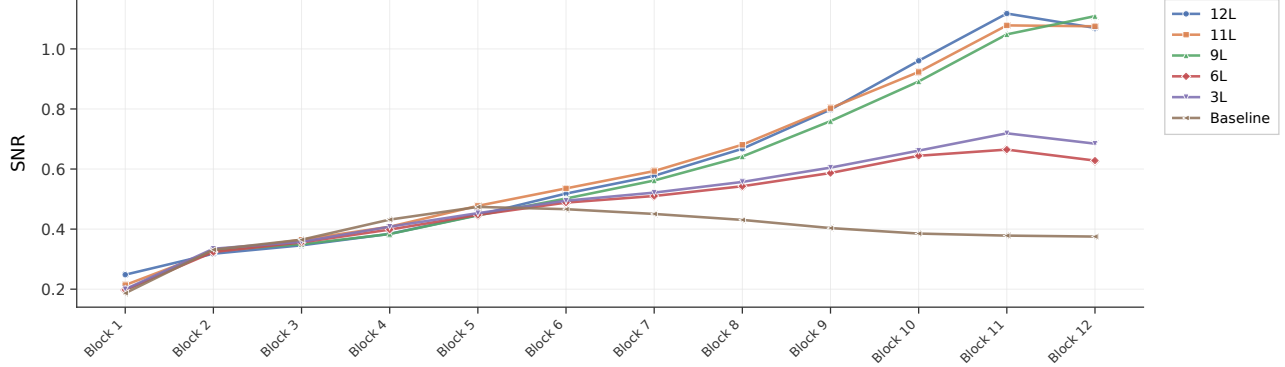


Figure 28. The Laplacian mechanism collapses tokens more effectively.

E. Results for Alternative Ways of Mixing Attention and the Laplacian Heads

Ignoring ordering, for a transformer with n blocks and h heads, there are in total $(h+1)^n$ possibilities of assigning Attention and \mathbf{L} to different heads, making it impossible to exhaustively try all options. Apart from the strategy described in the main paper, we tried:

- Only use Laplacian heads for the first half of the blocks, and only use attention for the second half. We refer to this option as "Mix-Depth".
- Alternate blocks that use only either attention or the Laplacian heads. We refer to this option as "Interleave".

Neither strategy performed noticeably better than the one we followed in the main paper, although they both improved upon the baseline. Interestingly, the order in which the two types of blocks is alternated appeared to impact performance, where the order Attention $\rightarrow \mathbf{L} \rightarrow$ Attention $\rightarrow \mathbf{L}$ performed worse than $\mathbf{L} \rightarrow$ Attention $\rightarrow \mathbf{L} \rightarrow$ Attention. More investigation is needed to understand these phenomena. We report the performance of these two options on ImageNet across different drop path rates in Table 4.

Table 4. Top-1 test accuracy (%) of models with different numbers of standard attention heads.

Model	ImageNet (dp = 0.1)	ImageNet (dp = 0.3)	ImageNet (dp = 0.4)
Baseline	79.39 ± 0.17	81.28 ± 0.01	81.54 ± 0.03
Mix Depth	80.66 ± 0.07	82.12 ± 0.03	82.42 ± 0.05
Interleave (attention first)	80.46 ± 0.09	82.21 ± 0.02	82.39 ± 0.06
Interleave (Laplacian first)	80.86 ± 0.09	82.41 ± 0.12	82.65 ± 0.26

F. Neural Collapse

F.1. Metrics

Let $M \in \mathbb{R}^{d \times C}$ be the matrix whose columns are the class means $\{\mu_i : 1 \leq i \leq C\}$ and $W \in \mathbb{R}^{C \times d}$ be the weight matrix of the final-layer classifier. We quantify NC2 - NC4 following (Han et al., 2022):

- **NC2 (Equinorm and Maximal Equiangularity):**

– *Equinorm*: Measures how uniform the vector norms are within the class means or weights, using the coefficient of variation (CoV):

$$\frac{\text{std}(\|\mu_c\|)}{\text{mean}(\|\mu_c\|)} \quad \text{and} \quad \frac{\text{std}(\|w_c\|)}{\text{mean}(\|w_c\|)},$$

where w_c is the classifier weight vector corresponding to class c .

- *Maximal Equiangularity*: Measures how close the vectors are to forming a maximally equiangular tight frame (ETF):

$$\frac{1}{C(C-1)} \sum_{i \neq j} \left| \langle \hat{v}_i, \hat{v}_j \rangle + \frac{1}{C-1} \right|,$$

where \hat{v}_i and \hat{v}_j are ℓ_2 -normalized class means or weight vectors. A lower value indicates greater conformity to an ETF structure.

- **NC3 (Self-Duality)**: Measures the alignment between the classifier weights and the centered class means:

$$\left\| \frac{W^T}{\|W^T\|_F} - \frac{M'}{\|M'\|_F} \right\|_F^2,$$

where $M' = M - \mu_G \mathbf{1}^T$ is the matrix of class means centered by their global mean μ_G .

- **NC4 (Convergence to NCC)**: Measures how close the learned classifier is to a Nearest Class Center (NCC) classifier:

$$1 - \frac{1}{N} \sum_{i=1}^N \mathbf{1} \left[\arg \max f(x_i) = \arg \min_c \|h_i - \mu_c\| \right],$$

where $f(x_i)$ are the logits, h_i is the feature of sample x_i , and μ_c is the mean feature for class c .

F.2. Visualization of Projection onto Simplex ETF

Each token embedding is first projected onto the classifier W for a random subset of three classes, then the result is projected again onto a two-dimensional representation of a three-dimensional simplex ETF. The result is visualized with each point colored according to its ground truth class. This visualization aims to illustrate the conformity of token embeddings to a simplex ETF.

Algorithm 2 Projection of Tokens to a simplex ETF

Require: $X \in \mathbb{R}^{B \times T \times d}$, $W \in \mathbb{R}^{C \times d}$

- 1: $X \leftarrow \text{reshape}(X, [B \cdot T, d])$, $W' \in \mathbb{R}^{3 \times d} \leftarrow \text{random sample}(W)$
- 2: $U, S, V^T = \text{SVD}(\text{normalize}(W'))$
- 3: $A \leftarrow \sqrt{2} \cdot \begin{bmatrix} \frac{1}{2} & -\frac{1}{2} & 0 \\ 0 & 0 & \frac{\sqrt{3}}{2} \end{bmatrix} \cdot (I_3 - \frac{1}{3} \mathbf{1} \mathbf{1}^\top)$
- 4: **return** $AUV^T X^T$
